2014

# A Feasibility Study of Ultra-Short Echo Time MRI for Positive Contrast Visualization of Prostate Brachytherapy Permanent Seed Implants for Post-Implant Dosimetry

Melissa Lamberto
*Louisiana State University and Agricultural and Mechanical College*

Follow this and additional works at: https://digitalcommons.lsu.edu/gradschool_theses

Part of the Physical Sciences and Mathematics Commons

A FEASIBILITY STUDY OF ULTRA-SHORT ECHO TIME MRI
FOR POSITIVE CONTRAST VISUALIZATION
OF PROSTATE BRACHYTHERAPY PERMANENT SEED IMPLANTS
FOR POST-IMPLANT DOSIMETRY

A Thesis

Submitted to the Graduate Faculty of the
Louisiana State University and
Agricultural and Mechanical College
in partial fulfillment of the
requirements for the degree of
Master of Science

in

The Department of Physics and Astronomy

by
Melissa Lamberto
B.S., University of the Sciences in Philadelphia, 2011
August 2014

ACKNOWLEDGMENTS

TABLE OF CONTENTS

# LIST OF TABLES

LIST OF FIGURES

ABSTRACT

Ultra-short echo time (UTE) imaging is a magnetic resonance imaging (MRI) technique that uses very short echo times (on the order of microseconds) to measure rapid T2 relaxation. An application of UTE is the visualization of magnetic susceptibility-induced shortening of T2 in tissues adjacent to metal, such as prostate tissue with implanted brachytherapy seeds. This study assessed UTE imaging of prostate brachytherapy seeds on a clinical 3T MRI scanner to provide images for post-implant dosimetry.

A prostate tissue phantom was made of gelatin mixed with Gd and other materials to mimic the prostate peripheral zone's T1 and T2 relaxation times; this phantom was used to investigate the effect of UTE acquisition parameters on brachytherapy seed visibility. A second phantom was made to model prostate tissue surrounded by muscle tissue; this pelvic phantom was implanted with 85 titanium brachytherapy seeds (STM1251, Bard Medical). Both phantoms were scanned on a 3T GE scanner with a 3D UTE pulse sequence and a fast spin echo (FSE) pulse sequence. The average seed SNR, the CNR between seed and prostate material, and visual characteristics of the seeds were assessed. A seed counting procedure was developed based on the visual seed characteristics, and subsequently used by two physicists to locate seeds in UTE images of the pelvic phantom.

On 3D UTE images, the metal seeds caused a bright ring-link artifact in adjacent prostate tissue due to susceptibility-induced T2 shortening. The average seed SNR was $15.99\pm1.52$ for UTE compared to $32.32\pm22.43$ for FSE; CNR between seed and prostate was $6.73\pm1.85$ for UTE vs. $23.76\pm12.87$ for FSE. The ring was larger in diameter than a seed itself; apparent seed diameters were $4.65\pm0.363$ mm for UTE compared to $1.46\pm0.38$ mm for FSE. The 3D spatial ring pattern facilitated differentiation of seeds from needle tracks and seed spacers. The two

physicists counted 83 and 86 seeds respectively in the UTE images. Prostate boundaries were less well visualized with UTE compared to FSE.

With its ability to visualize brachytherapy seeds, UTE imaging appears to provide an alternative approach to CT for seed identification. Compared to fusion of separately-acquired CT images and T2-weighted MR images (for delineation of prostate boundaries), UTE and T2-weighted MR can be acquired in a single imaging session – a convenience to patients while potentially minimizing inter-modality image registration issues. A study in prostate brachytherapy patients of the quality of post-implant dosimetry with UTE imaging compared to CT imaging is recommended.

CHAPTER 1: INTRODUCTION

1.1  Overview

The goal of this project was to investigate the feasibility of an ultra-short echo time (UTE) magnetic resonance imaging (MRI) pulse sequence for localization of permanent brachytherapy seeds. UTE is a pulse sequence that provides a unique perspective on imaging seeds after implantation due to the positive contrast of metal compared to tissue in UTE images. This thesis summarizes the theory of UTE and the artifacts produced when metallic objects are imaged. Possible limitations inherent in the UTE technique are discussed. This project utilized phantom studies to evaluate the possibility of implementing UTE for post-implant seed localization in clinical practice for prostate brachytherapy.

1.2 Current State of Prostate Cancer Treatment

The prostate is a male genitourinary gland located in the pelvis (Figure 1.1). According to the 2012 SEER report, one in seven American men will be diagnosed with prostate cancer in his lifetime; prostate cancer is the second most common cancer among men in the United States after skin cancer (Howlader 2013). There are various treatment options for these men depending on the extent of their cancer at presentation.

Of the men diagnosed with prostate cancer annually, 81% have disease that is confined within the prostate capsule (Howlader 2013). Permanent prostate brachytherapy (PPB) monotherapy is suggested as a standard-of-care treatment option for these low-risk (Gleason 3+3, PSA <10 and T1c or T2a) patients (Davis 2012). Low intermediate risk (usually only one of: Gleason 3+4, PSA 10-20, T2b or T2c) patients are regarded by many physicians as candidates for monotherapy. Higher risk patients may be candidates for PPB implant as a boost with external beam radiotherapy.
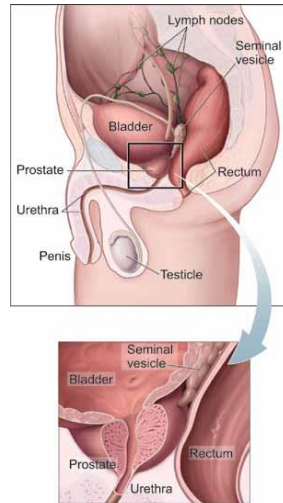
Figure 1.1: Illustration of prostate anatomy. (top) A sagittal view of the male pelvis with the prostate highlighted in the red box. (bottom) The enlarged view shows the bladder and rectum in relation to the healthy prostate (CDC 2013).

1.3 Permanent Prostate Brachytherapy

Permanent prostate brachytherapy is low dose rate, "sealed-source" radiotherapy. It is a cancer treatment technique that requires a physician to implant radioactive, cylindrical sources, called seeds (Figure 1.2), into the patient's prostate. The seeds remain in the patient indefinitely.



Figure 1.2: Photo of a typical brachytherapy seed (Bard Medical, Inc.) used in permanent prostate brachytherapy. The seed capsule is made of titanium, about 4.5 mm long by 1 mm in diameter as seen on the ruler.

Low dose rate radioactive materials commonly used for this procedure are iodine-125 and palladium-103. Different designs are available from the various manufacturers (see Section 3.2.4

for a discussion of the design used in this project). Implantation of these seeds into the prostate is planned so that a prescribed therapeutic dose is delivered to the prostate itself while dose to the surrounding tissues, i.e. rectum and bladder, is minimized.

1.3.1 Steps of the LDR prostate brachytherapy procedure

A typical prostate brachytherapy procedure is completed in three steps: (1) pre-treatment planning, (2) implantation of radioactive seed sources, and (3) evaluation of the quality of the implant. Each part of this process relies heavily on imaging to ensure a quality procedure that delivers the desired dose.

In the first step, the prostate is imaged with trans-rectal ultrasound (TRUS) and a pre-plan is generated. The physician contours the prostate as well as the organs at risk, which include the urethra, bladder, and rectum. For monotherapy PPB, the typical prescribed dose is 125-145 Gy depending on the selected radioactive source. The dosimetrist or physicist maps out where the seeds should be placed to achieve the best possible dose coverage of the prostate while minimizing the dose to the rectum, bladder, and urethra. As recommended by the American Brachytherapy Society, the entire prostate volume must be covered by 100% of the prescribed dose, while the urethra should not exceed 150% of the prescribed dose (Nag 2000, Tempany 2012).To achieve the desired dose coverage, seeds are usually placed peripherally in the prostate to maximize the dose to the whole gland while minimizing the dose to the centrally located urethra. The plan ideally limits dose to the rectum and bladder immediately adjacent to the prostate. This pre-plan determines the number of seeds needed for a successful implant; typically, around 100 seeds are implanted within a 40-60 cc prostate.

In the second step, the physician implants the seeds by hand using TRUS image guidance (Figure 1.3). Seeds are loaded in needles for implantation. A typical implant uses about 20

needles and takes approximately 1-2 hours in an outpatient setting. When estimating the dose coverage, the physician must consider error associated with the hand placement technique. Many physicians overestimate the dose coverage by about 2 mm outside of the entire prostate (Tempany 2012). Also, the prostate swells due to the needle insertions which may cause movement of seeds after placement in the prostate.
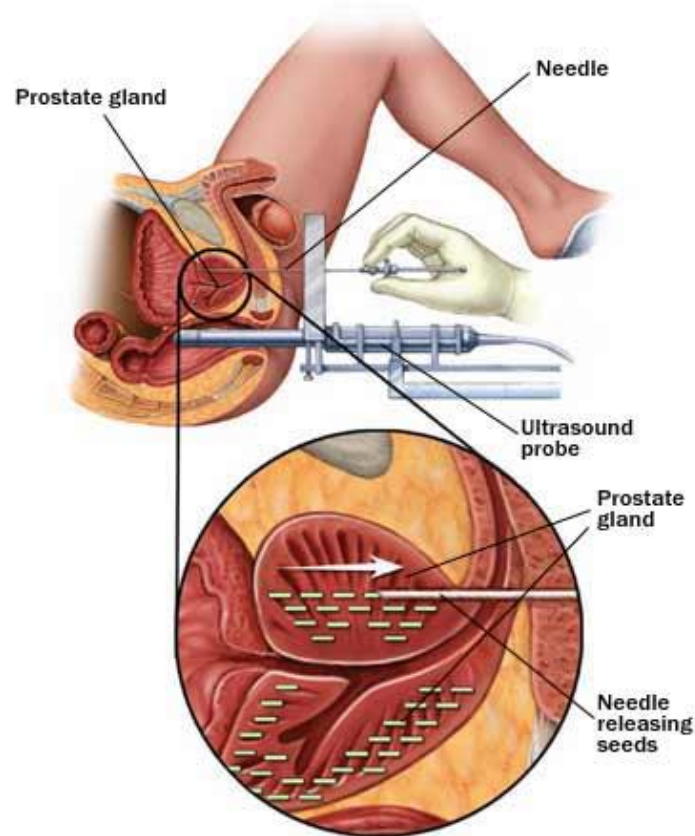


Figure 1.3: Illustration of a prostate brachytherapy procedure (Mayo Foundation for Cancer Research).

In the final step of the process, the patient returns for a follow-up visit approximately 30 days after implantation, which allows time for swelling to abate. This part of the procedure, called post-implant dosimetry, is typically performed with computed tomography (CT) images. The pelvis is imaged, the seed locations are identified, and the delivered dose is re-calculated

according to the seed positions relative to the prostate contour. This post-plan is used by the physician to assess plan quality and overall success. Furthermore, if the delivered dose is insufficient, supplemental treatment options can be recommended.

1.3.2  Importance of post-implant dosimetry

Considering the errors possible from the hand delivery technique, re-calculating the delivered dose is crucial to estimate actual dose coverage. While the main purpose of post-implant dosimetry is to assess the quality of the delivered plan, it also provides quality assurance for future implant procedures by helping the physician improve his or her technique. With high quality post-implant dosimetry, physicians can analyze the procedures to determine correlations between treatment delivery, patient morbidity, and tumor control.

1.3.3  Requirements for post implant dosimetry images

Post-implant dosimetry is a critical step in the brachytherapy process, but currently has several shortcomings which lead to uncertainty in treatment outcomes.  Current brachytherapy treatment guidelines mandate the use of an acceptable imaging modality for seed localization and prostate delineation for post-implant dosimetry calculations. CT is the common modality, currently. For post-implant images to be clinically useful, the image must:

(1)show the locations of the implanted seeds;

(2)show the outline of the prostate for calculations; and

(3)provide a realistic representation of the internal anatomy (with minimal spatial distortions)

Fortunately, post-implant dosimetry uses a dose calculation formalism that does not require electron density to determine delivered dose (Rivard 2004). Unlike the majority of radiation planning scenarios, brachytherapy delivers dose at short range to tissues with similar electron densities. According to the Task Group 43 guidelines from the American Association of

5

Physicists in Medicine (Nath 1994), the delivered dose is determined by approximating the tissue density to be water-equivalent throughout the patient. Essentially all tissue inhomogeneities can be ignored (Rivard 2004).This means that a variety of imaging modalities, besides CT, could be used for dose calculation, as long as that image source provides accurate locations of the seeds with respect to the prostate volume. Determining a true prostate outline provides a precise treatment evaluation which, as discussed previously, should lead to improvements in future treatment accuracy and aid in prediction of side effects from the procedure.

1.3.4  Current state of CT for post-implant dosimetry

Although the recommended treatment guidelines state that CT is a useful modality for post-implant dosimetry calculations, poor visibility of both prostate and seeds on a CT image causes uncertainty in the re-calculated delivered dose (Lindsay 2003, Crook 2010). One issue that occurs with CT imaging is the presence of streaking artifacts due to the high Z material of the seed (Figure 1.4). This leads to artifacts on the post-implant image which degrade the accuracy of dosimetry calculations (Dubois 2001, Lindsay 2003).

Published studies show that using CT images for post-implant dosimetry often lead to overestimation of the prostate volume due to the physician's disrupted view of the prostate from seed artifacts (Bowes 2013). Additionally, inter-observer variability increases when prostate volumes are contoured on CT images (De Brabandere 2012). This is illustrated in Figure 1.5, where 3 prostates were contoured by 7 inexperienced physicists on selected CT slices, as compared to the reference prostate contour delineated by two experienced physicists.

6
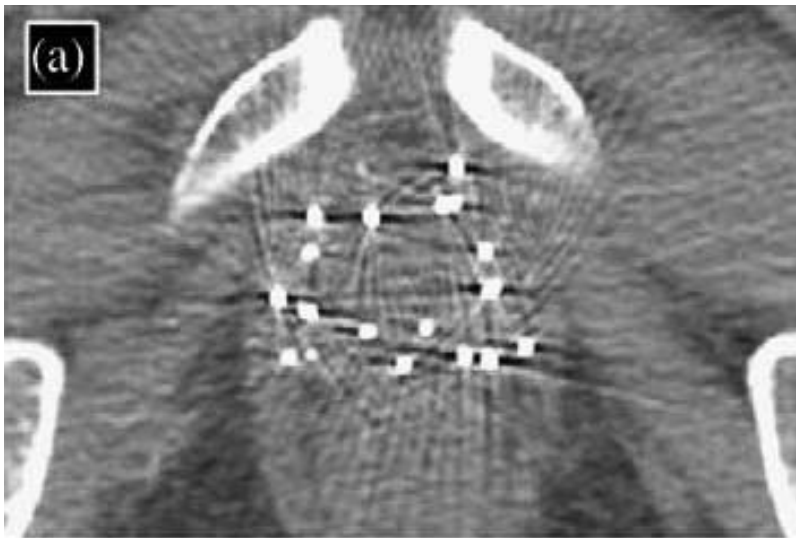
Figure 1.4: CT image of pelvis with seeds implanted into prostate (De Brabandere 2006).
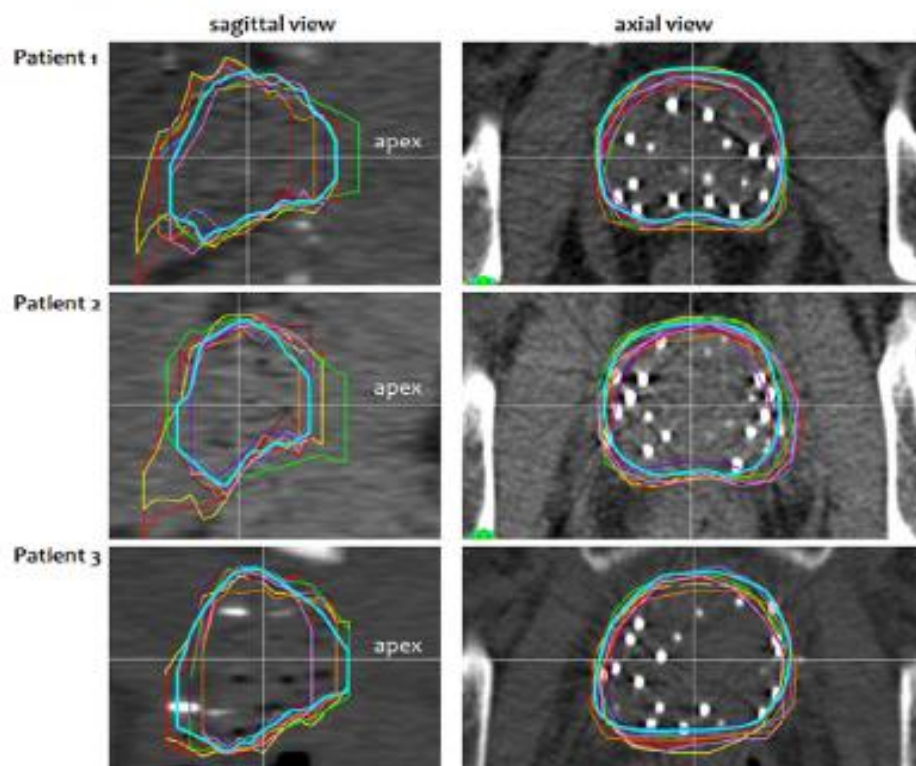


Figure 1.5: Prostate contours drawn on CT by 7 observers selected for their inexperience in contouring prostates (De Brabandere 2012). The blue contour was the reference prostate contour confirmed by two experienced physicists using MRI. The lines shown in other colors were the contours drawn by the 7 inexperienced observers.

1.3.5 Current state of MRI for post-implant dosimetry

An alternative imaging method for post-implant dosimetry is MRI. MRI doesn't suffer from streak artifacts like CT. Due to the inherent magnetic properties of metal, metal is overall poorly visualized via MR (Figure 1.6), and may introduce susceptibility artifacts that affect the visualization of the surrounding tissues. When using MR imaging after implantation, prostate visibility should be improved compared to CT, but localization of seeds may or may not be better (Katayama 2011, Bowes 2013).
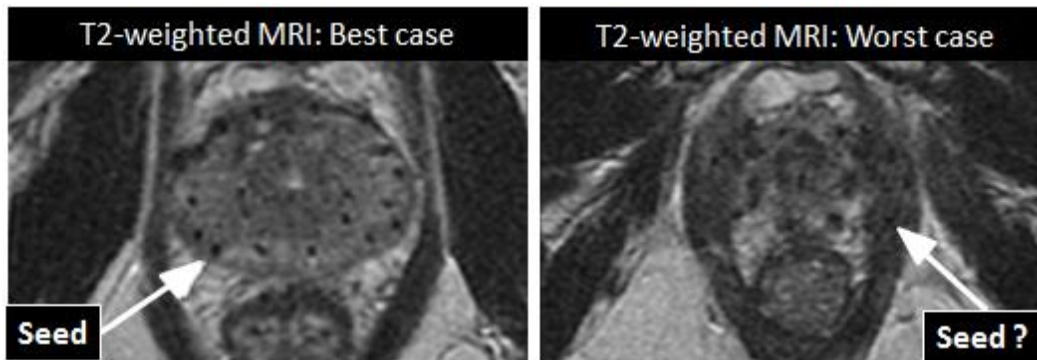


Figure 1.6: Best (left) and worst (right) case display of seed visibility on MR-based post-implant dosimetry images (Brown 2013).

1.3.6 Previously published studies using MR-based post-implant dosimetry

Few articles have been published investigating MR alone, compared to fused CT/MR or CT alone for post-implant dosimetry. Some institutions implement the use of CT post-implant images fused with MR post-implant images (Crook 2010, Bowes 2013). The two images are fused to exploit the benefits of each modality while simultaneously compensating for their disadvantages (Figure 1.7). This has become the gold standard for post-implant dosimetry, although the current guidelines do not specifically require combining the two types of images.

De Brabandere (2012) compared prostate contouring between CT, MR, and fused CT/MR images (cf. Figure 1.5). The reported inter-observer variability for the dose to 90% of the

contoured prostate volume (D90) based on seed localization from the CT image was 2% variation, while the D90 varied by 7% for the use of MR-based seed localization. In the image fusion-based localization study, the D90 varied by 2% as well.
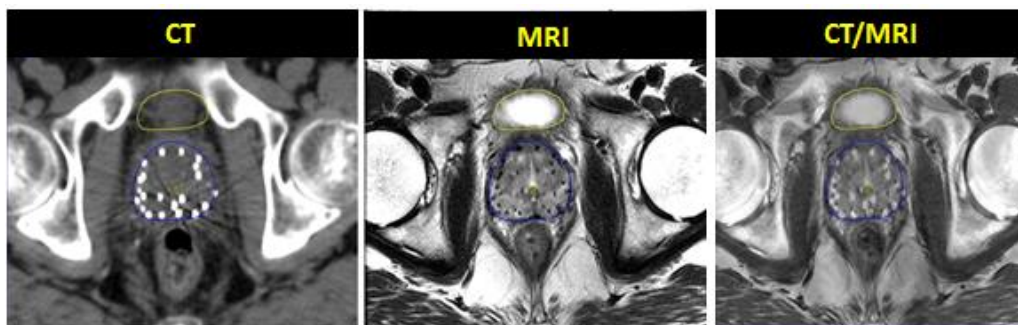


Figure 1.7: (Left) CT, (middle) T2-weighted MRI, and (right) CT/MR fused post-implant images of a prostate with contours drawn from the MRI overlaid onto the CT and CT/MR images. (Brown 2013)

Unfortunately, MR/CT fusion can be difficult, due to distortion of the MR images from various factors. Also, obtaining both types of images may be impractical for some facilities. For example, an MRI scanner may not be available onsite; off-site MR imaging would require a separate patient appointment. From a patient's perspective, convenience dictates using a single imaging modality for post-implant dosimetry. MR imaging provides good visualization of the prostate, but using it to visualize seeds is an area needing further exploration.

Tanaka et al (2006) investigated the use of T2, T1, contrast enhanced, and fat suppressed T1 images. They concluded that MR-based dosimetry was adequate for prostate contouring, but seed localization was inadequate. Other authors investigated the possibility of fusing T2-weighted and T2*-weighted MR images (Figure 1.8) to create a final post-implant dosimetry image (Katayama 2011). The main error discovered by this technique involved the localization of seeds outside of the prostate within the pelvis (cf. Figure 1.6). The seeds were difficult to visualize due to the fact that inherent inhomogeneities in the pelvic region appear similar on MR

image to those introduced by the seeds. These inhomogeneities included hemorrhages, calcifications, blood vessels, and air bubbles. The results suggested that MR-based dosimetry is possible, but a better pulse sequence may be necessary to extract the seed locations from the MR image.
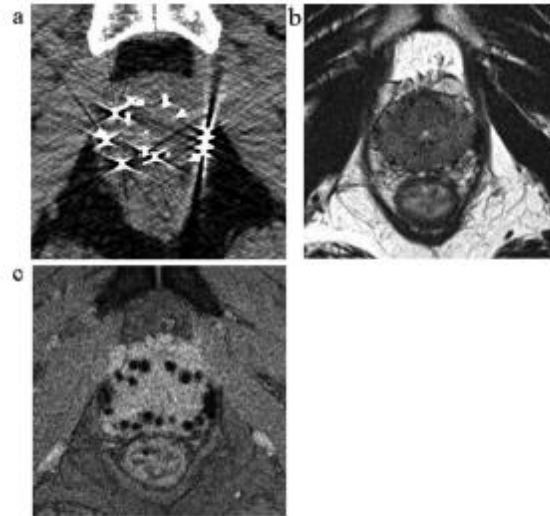


Figure 1.8: Axial slice post-implant images of the prostate corresponding to (a) CT, (b) T2-weighted MRI, and (c) T2*-weighted MRI (Katayama 2011).

1.3.7 Susceptibility mapping for seed localization

A pulse sequence that could lead to improved seed detection is susceptibility mapping. (Chapter 2 provides a review of MR physics including the concept of susceptibility). The magnetic susceptibility of the metal seeds alters local magnetic field strength; adjacent tissues exhibit a different resonance behavior than distant tissues. Specifically, the metal seeds cause a spatial variability in the local tissue relaxation rates (Haacke 1999). This phenomenon can be exploited with a type of image sequence called susceptibility mapping. Susceptibility mapping identifies metallic objects by mapping out the magnetic field changes due to the metal. Ideally, non-metallic objects don't alter susceptibility so only the location of the metal seeds would be identified.

Susceptibility mapping can be further enhanced to achieve visual seed distinction, called positive contrast. Essentially, the protons that produce an on-resonance signal (e.g., those from non-metal material) are suppressed. The scanner only reads the signals that occur off-resonance, at a shifted frequency that corresponds to the altered local magnetic field strength in the vicinity of the metal seeds. One group has published promising phantom results that show this concept is feasible to locate seeds within the prostate area (Kuo 2010). Extra-prostatic inhomogeneities were ignored in this study.

1.4 Goal, Hypothesis, and Aims

The goal of this project was to identify and assess an MRI pulse sequence that could distinguish permanently implanted prostate brachytherapy seeds from their surroundings. An ideal sequence would visualize all seeds, i.e. with high contrast vs. prostate, and would allow the seeds to be differentiated from air cavities or other confounding structures. An ideal sequence also would be able either to visualize the prostate boundaries within the pelvis or to have minimal spatial distortions to facilitate registration with other MRI scans or CT.

We hypothesized that a 3D ultra-short echo time (UTE) pulse sequence will provide MR images of permanent brachytherapy seeds with positive contrast, defined as seed signal that is statistically larger than the prostate signal ($p < 0.05$). The seeds also will be distinguishable from air on the UTE images, meaning the signal from metal will have a signal that is statistically different than the signal from air cavities within the prostate ($p < 0.05$).

This project was executed through the completion of three aims. The following chapters provide a review of MR imaging concepts, including the UTE pulse sequence, and address the approach and results for each aim.

Aim 1, Phantom Development: Develop a phantom with magnetic resonance behavior that

      models human prostate tissue at 3T, which can be implanted with brachytherapy seeds.

Aim 2, Image Acquisition and Quality Assessment: Acquire images with a selection of 3D UTE

      pulse sequence parameters that provide positive seed contrast. Analyze these images for

      several image quality metrics.

Aim 3, Seed Localization Procedure and Reconstruction Accuracy: Create a procedure for

      identifying the locations of seeds in UTE images. Have two physicists use the procedure

      to identify and locate seeds in a pelvis phantom.

CHAPTER 2: BACKGROUND

2.1 Overview

This chapter reviews concepts about magnetic resonance imaging that are relevant to an understanding of this thesis.

2.2 MR Physics Review

Magnetic resonance imaging (MRI) is a non-invasive imaging technique that exploits the nuclear magnetic resonance behavior of atoms to gain spatial information about their environment. Nucleons (protons and neutrons) possess spin angular momentum, giving each a magnetic moment. Atoms with an odd atomic mass, like hydrogen, possess a non-zero net nuclear magnetic moment, generically called a "spin". When placed in an external magnetic field of strength $B_0$, the spins precess at the Larmor frequency, $\omega_0$, as

$$\omega_0 = \gamma B_0. \tag{2.1}$$

The gyromagnetic ratio, $\gamma$, is a constant that is characteristic of the atom; typical units are MHz/T. The external or static $B_0$ field is generated by the MRI scanner. While in the static field, each hydrogen spin acts as a dipole magnet. Each spin occupies either a low energy "spin-up" state (when the dipole aligns with $B_0$) or a high energy "spin-down" state (when the dipole aligns opposite to $B_0$). The vector sum of the diploes along $B_0$ (designated as the longitudinal axis) is the net longitudinal magnetization vector, $M_z$, illustrated in Figure 2.1a (Hornak 2014). At equilibrium (Figure 2.1b), this net magnetization vector reaches a maximum value, $M_0$, indicating the largest possible number of spins are located in the spin-up state.

In a magnetic field, the spins in different materials behave in unique ways. For instance, fat appears different than cartilage or muscle due to differing degrees of spin interactions in these tissues. To collect information about the environment of the spins, a radiofrequency (RF) pulse is

applied to the imaging volume to perturb the dipole moments, effectively pushing their alignment away from $B_0$. After the RF pulse, the net magnetization vector returns over time to the equilibrium state (Figure 2.1c). The rate of return is determined by the interactions of the spins with each other and with the local molecular environment. The interactions are exponential processes characterized by tissue-specific time constants.
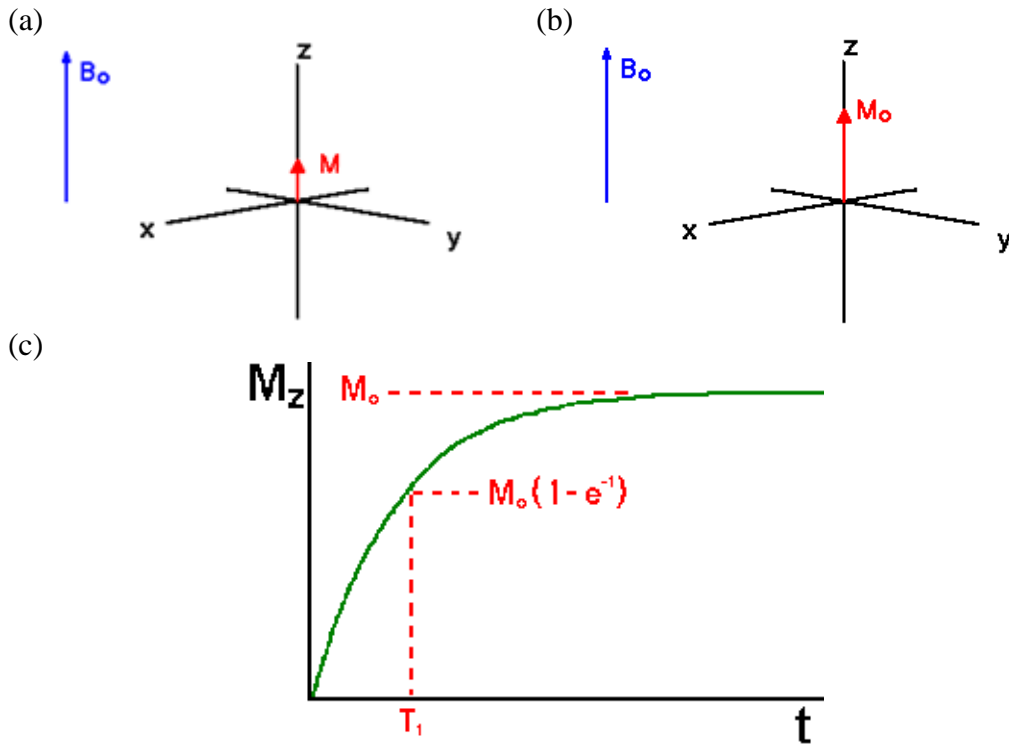


Figure 2.1: (a) Vector sum of dipole spins along $B_0$, defined as the longitudinal axis, produce the net magnetization vector, M. (b) At equilibrium, the net magnetization vector achieves a maximum value, $M_0$. (c) Longitudinal (T1) relaxation of the net longitudinal magnetization vector; $M_z$ grows exponentially to equilibrium with a time constant T1 (Hornak 2014).

## 2.2.1 T1 relaxation

Spin-lattice relaxation describes the rate at which the longitudinal magnetization vector re-grows over time (Figure 2.1c), given by

$$M_z(t) = M_0 \left(1 - e^{-\frac{t}{T_1}}\right) \qquad (2.2).$$

14

where T1 is the spin-lattice relaxation time constant, $M_0$ is the equilibrium magnitude, and t is the time since the perturbation by the RF pulse. T1 relaxation occurs as spins exchange energy with the environment (lattice) to move from the spin-down state to the spin-up state.

2.2.2 T2 and T2* relaxation

The magnitude and duration of the perturbing RF pulse determines the amount by which the net magnetization vector is pushed away from the longitudinal axis, typically expressed in degrees of rotation from the z-axis. A common pulse magnitude is 90°, which rotates M into the transverse plane (Figure 2.2a). M rapidly loses phase coherence in the transverse plane, illustrated in Figure 2.2b.
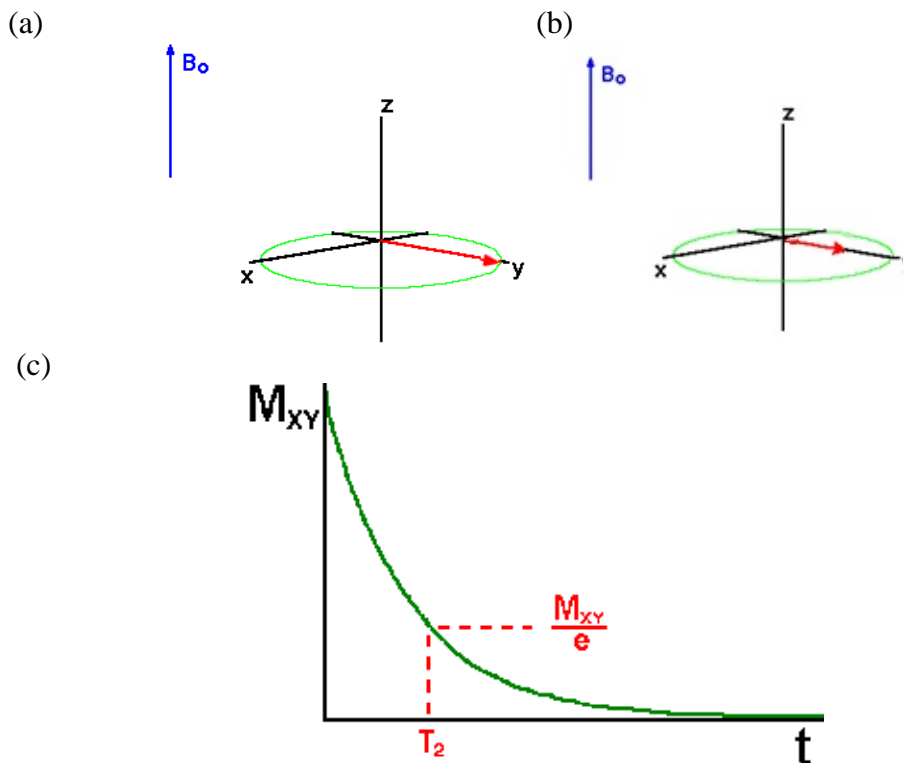


Figure 2.2: (a) Net magnetization vector rotated into the transverse plane following a 90° RF pulse. (b) Dephasing of the transverse magnetization. (c) Transverse (T2) relaxation of the net transverse magnetization vector; $M_{xy}$ decays exponentially with a time constant T2 (Hornak 2014).

The T2 time constant represents the rate of decay of the transverse magnetization vector due to phase loss during spin-spin interactions. Also termed spin-spin relaxation, T2 relaxation is illustrated in Figure 2.2c and described by

$$M_{xy}(t) = M_{xy}(0)e^{-\frac{t}{T2}} \tag{2.3}$$

where $M_{xy}(0)$ is the magnitude of the net magnetization in the transverse plane, immediately after the RF pulse has been applied, and T2 is the spin-spin relaxation time constant.

A second contributor to the loss of transverse magnetization is T2* decay, which represents loss of phase coherence of the spins due to inhomogeneities in the $B_0$ field (Figure 2.2b). The T2* time constant folds together the T2 and inhomogeneity relaxation effects as

$$\frac{1}{T2^*} = \frac{1}{T2} + \frac{1}{T_{inhomogeneity}} = \frac{1}{T2} + \gamma\Delta B_0 \tag{2.4}$$

where $\Delta B_0$ represents the magnitude of $B_0$ field inhomogeneity. Large inhomogeneities result in short T2*, masking the T2 relaxation of the spins. This results in a rapidly disappearing signal that may cause signal collection difficulties (Figure 2.3).
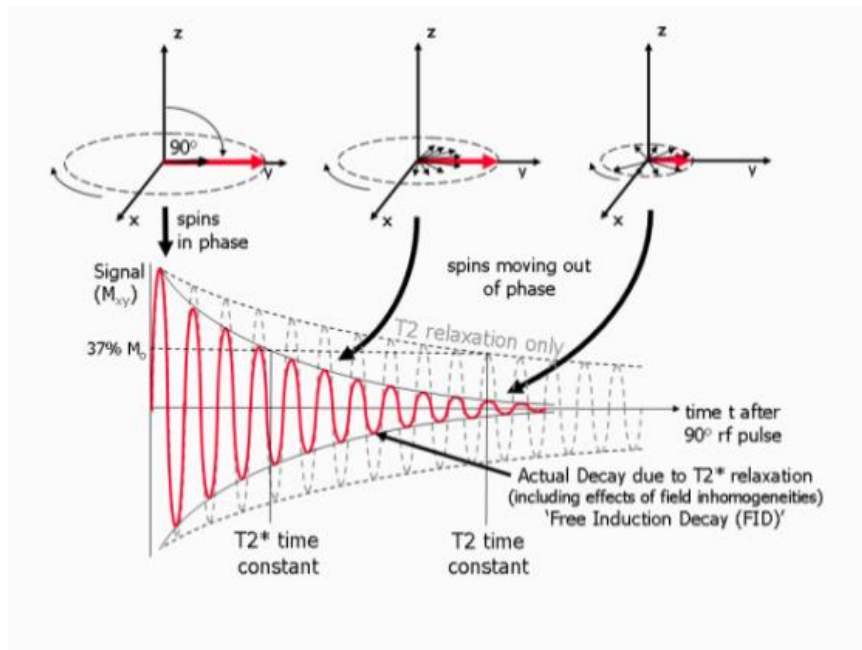


Figure 2.3: T2 and T2* relaxation of the transverse magnetization vector (Ridgway 2010).

<u>2.2.3 T1 and T2 for prostate tissue</u>

The T1 and T2 relaxation rates are unique to a specific tissue when placed in a magnetic field, although T1 depends on $B_0$ while T2 does not. The time constants for prostate tissue at 3T are approximately T1=1597 ms and T2=74 ms (Hattori 2013). The T2 relaxation rate varies depending on the location of the prostate tissue within the whole gland: central gland T2=78 ± 8 ms, peripheral zone T2=114 ± 27 ms, tumor T2=82 ± 15 ms (Foltz 2013). The relaxation time constants for a material are determined by measuring signal intensity at various points in time.

<u>2.3 Pulse Sequence Diagrams and Acquisition Parameters</u>

A pulse sequence diagram describes the series of events that occur during an MRI scan. A gradient recalled echo pulse sequence diagram is shown in Figure 2.4. When collecting a signal, the user defines the acquisition parameters of the pulse sequence to emphasize a particular component of relaxation. User-defined variables include echo time (TE), repetition time (TR), slice thickness, flip angle, receiver bandwidth, field of view, pixel size, frequency encoding gradient, phase encoding gradient, step sizes, direction, and number of measurements or excitations per voxel. These parameters are discussed when appropriate in the following sections, in addition to the following definitions:

a) Field of view (FOV) is the distance across the image in the frequency encoding direction.

b) Receiver bandwidth (rBW) is the range of frequencies accepted by the receiver coil.

c) Flip angle is the angle by which the net magnetization vector ($M_0$) is rotated or perturbed from the longitudinal axis.

d) K-space is the coordinate space covered by the phase and frequency encoding gradient data; k-space is the Fourier transform of image space.
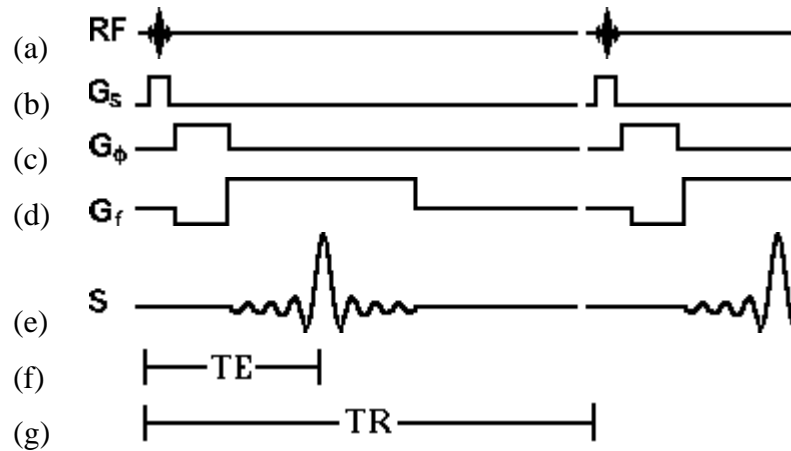
Figure 2.4: Pulse sequence diagram for a gradient recalled echo (Hornak 2014). (a) The RF pulse perturbs the net magnetization vector (M) from the equilibrium position; the flip angle, in degrees of rotation from $B_0$, is determined by the strength and duration of the RF pulse. (b) The slice selection gradient $G_s$ determines the imaging plane and governs the slice thickness of the image. (c) $G_\phi$ is the phase encoding gradient used to alter the phase angle of the spins as a function of position. (d) $G_f$ is the frequency encoding gradient which alters the spins' precession frequency as a function of position orthogonal to $G_\phi$. The frequency encoding gradient forces an echo to form for signal collection. (e) S is the echo signal produced by the spins, collected by receiver coils; S represents the spatial composite of the frequencies and phases of the spins, which is inverse Fourier transformed into the image. (f) Echo time (TE) is defined as the time between the center of the RF pulse and the center of the echo. (g) Repetition time (TR) is the time to complete one full cycle of the pulse sequence.

e) Number of excitations (NEX) determines the number of times each line of k-space is sampled; NEX is the number of repeat measurements used to decrease image noise.

2.4 Magnetic Susceptibility

Magnetic susceptibility is the ability of a metal to become magnetized when placed in a magnetic field. Highly susceptible ferromagnetic materials interact strongly with external magnetic fields. Ferromagnetic metals become magnetized because of their large susceptibility and may exhibit permanent magnetization; ferromagnetic materials are unsafe for MRI. Because of their weak susceptibility, paramagnetic materials and diamagnetic materials are only slightly magnetized compared to ferromagnets. Paramagnetic and diamagnetic metals do not remain magnetized when removed from the external magnetic field. Both types of materials alter the

external magnetic field in their vicinity (Figure 2.5); paramagnetic metals such as titanium concentrate the magnetic field lines in their vicinity.
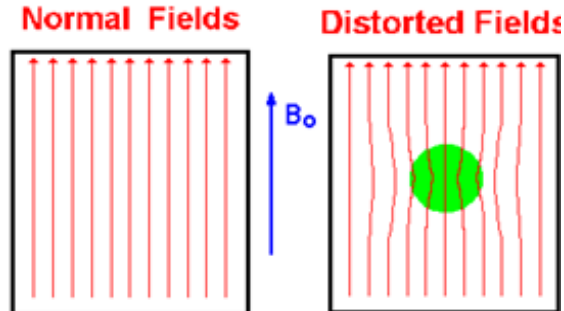


Figure 2.5: Static field ($B_0$) distortion due to the presence of a paramagnetic metallic sphere (Hornak 2014).

2.5 Phase Difference Mapping

Phase difference maps (Figure 2.6) are a convenient way to visualize the $B_0$ distortions caused by the presence of paramagnets in a magnetic field. The values in the phase map represent frequency differences from the Larmor frequency ($\omega_0$); frequencies higher or lower than $\omega_0$ are due to relatively increased or decreased local magnetic field strength, respectively. The apparent abrupt transitions (from dark to bright) in the phase map, called phase wrapping, are because frequency shifts have a period of $2\pi$. The phase differences reveal information about $B_0$ inhomogeneities because of its effect on T2* relaxation.
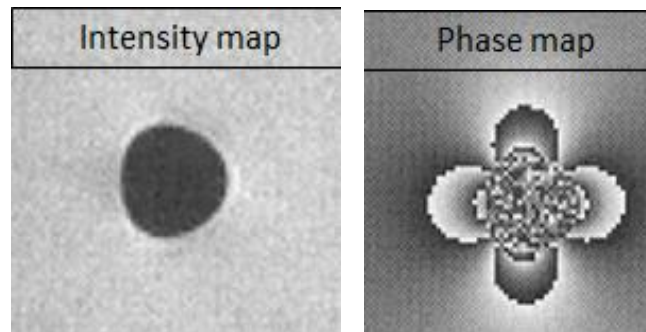


Figure 2.6: Intensity map and phase map of a metallic sphere in a gelatin phantom (Haacke 1999). In these images, the $B_0$ field points from bottom to top. Distortions in the intensity map are due to right-left orientation of the frequency-encoding readout gradient.

2.6 Ultra-short Echo Time Pulse Sequence

Tissues with a short T2 time constant lose their signal rapidly; additional T2* shortening further increases the rate of signal loss. Figure 2.7 compares the magnitudes of transverse signal over time for short T2 and long T2 materials. If the acquisition TE is long compared to the short T2 (or T2*), as in Figure 2.7(top), the signal from the short T2 material will be completely decayed by the time of signal acquisition. This material will not appear in the collected image. Using a shorter TE allows the signal from rapidly decaying tissues to be collected and therefore represented on the MR image, as shown in Figure 2.7 (bottom).
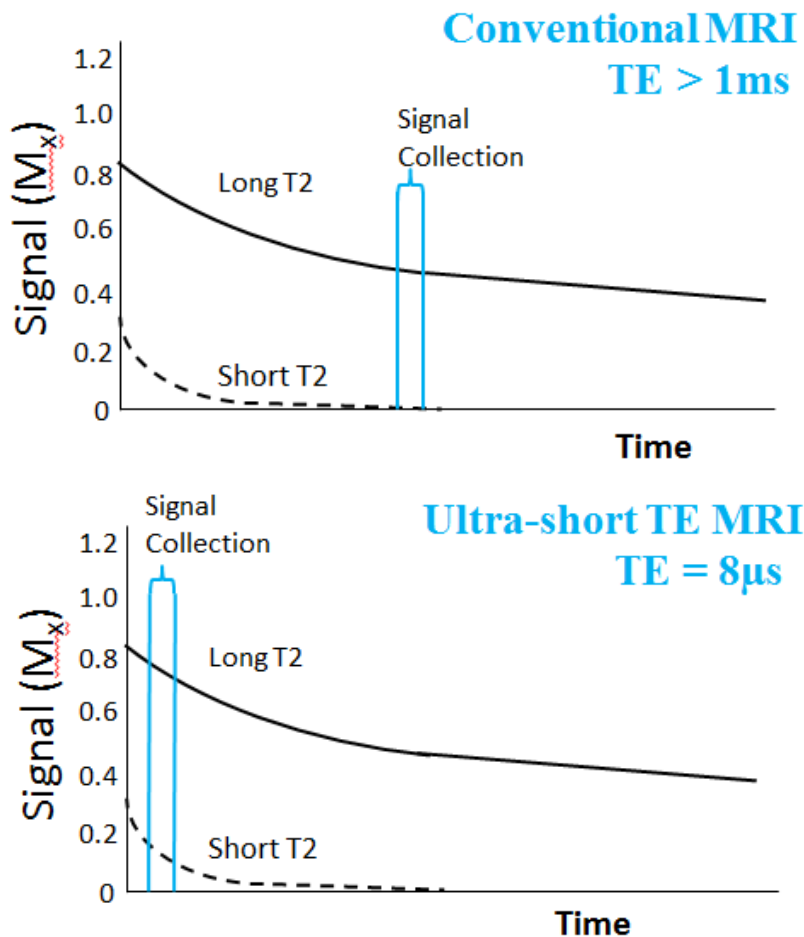


Figure 2.7: Transverse magnetization decay for short T2 and long T2 materials. (top) With a long TE (conventional MRI), no signal remains from the short T2 material. (bottom) With a short TE (UTE MRI), signal can be collected from the short T2 material.

A reduction of TE imposes critical restrictions on the pulse sequence parameters, such as limiting the flip angle (with short RF flip pulses) or using separate coils for RF generation and signal reception. The main feature of the UTE pulse sequence is the ability to collect a signal about 1 order of magnitude faster than the fastest TE available on conventional MRI scanners (Robson 2003, Bydder 2012).

2.6.1 Features of UTE pulse sequence

Extremely short TE acquisition imposes restrictions on the pulse sequence parameters. These parameters influence image quality and overall imaging time, as well as pushing the limits of the scanner hardware. The UTE pulse sequence investigated in this project was a 3-dimensional scan. The 3D UTE scan produces isotropic resolution. This is advantageous to localize fine details on an image, e.g., titanium seeds for the current project.

The UTE sequence uses radial filling of k-space to achieve isotropic resolution and rapid acquisitions (Figure 2.8). With radial acquisition, the spatial encoding gradients rotate in orientation relative to the coordinate system of the image slice. This results in susceptibility artifacts with radial symmetry rather than the left-right symmetry shown in the phase map of Figure 2.6 where the readout direction was only in the horizontal direction. This has implications for the appearance of brachytherapy seeds, as discussed in section 5.2.2.

2.6.2 Previous studies of UTE imaging of metal

A study by Carl et al. (2013) highlighted the ability of the UTE sequence to preserve signal from tissue adjacent to metal that would otherwise be lost from rapid T2* de-phasing of the transverse signal. An interesting characteristic was noted when ultra-short echo times were used for signal acquisition. Very short TE caused a large displacement of signal (red arrows in Figure 2.9) while a longer TE caused a loss of signal (blue arrows) at the boundary of two

materials with substantially different magnetic susceptibilities. This characteristic contributes to

the utility of UTE for imaging patients with metallic implants (see Chapter 4).
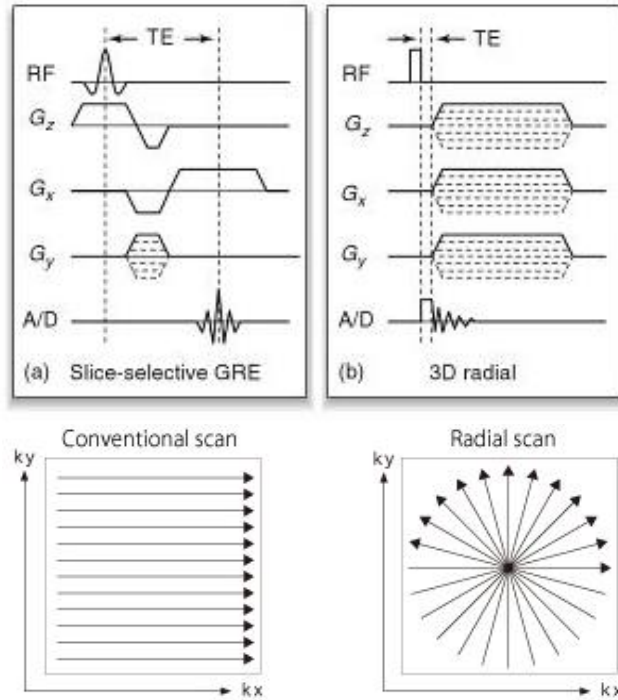


Figure 2.8: (top) Pulse sequence diagrams of a gradient echo pulse sequence that uses (left) a static orientation of the readout gradients and (right) a 3D radial orientation of the readout gradients (Bydder 2012). (bottom) Illustration of k-space filling in 2D by each acquisition method (Hitachi Medical Corporation 2014).
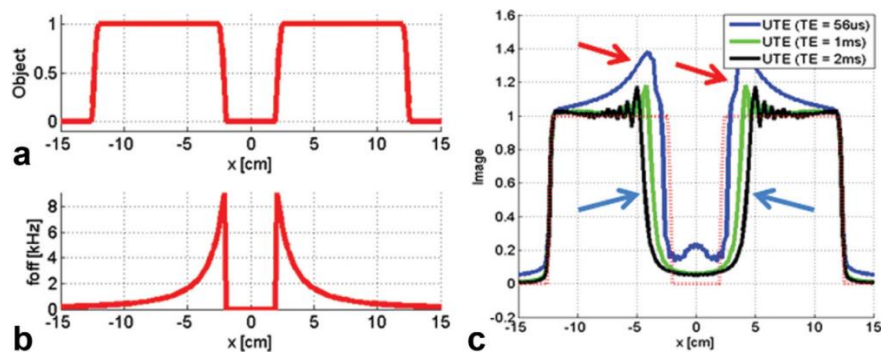


Figure 2.9: Observed signal locations (blue, green and black lines) compared to actual signal, shown as red lines in (a) and (c), of spins adjacent to a 2.5-cm metal block. Signal pile-up (red arrows) or loss (blue arrows) was seen with shorter or longer echo times within the UTE sequence (Carl 2013). The red line in (b) illustrates the relative increase in local magnetic field due to susceptibility.

CHAPTER 3: AIM 1, PHANTOM DEVELOPMENT

3.1 Overview

The goal of this aim was to develop a phantom that modeled human prostate tissue on a 3T MRI scanner. With implanted brachytherapy seeds, the phantom should produce images suitable for assessing the appearance of brachytherapy seeds on UTE images.

As explained in Section 2.2.3, a T1 time constant of 1597 ms and a T2 time constant of 74 ms were the target values to model prostate tissue at 3T (Hattori 2013). To determine the correct recipe, a series of twelve material compositions were tested; the T1 and T2 time constants were evaluated for each. Of this series, four prostate phantom compositions closest to the target T1 and T2 values were selected for the fabrication of a larger pelvic phantom to model a prostate surrounded by non-prostate material in a region approximately the size of the adult male pelvis.

This chapter first describes the survey of material compositions, including the steps to prepare the materials and the subsequent validation of the T1 and T2 values. Next, the fabrication of the pelvic phantom is detailed. Finally, the process of seed implantation is described including the acquisition of phase maps to assess $B_0$ distortion by the titanium seeds.

3.2 Survey of Material Compositions

3.2.1 Target T1 and T2 time constants

The T1 and T2 time constants suggested by Hattori et al (2013) for prostate tissue were T1=1597 ms and T2=74 ms. Other authors have reported a wide range of values for prostate tissue T2 values. The average reported value for healthy prostate tissue in the central gland of the prostate was a T2 time constant close to 80 ms, while cancerous tissue had a T2 time constant anywhere from 82 ms to 110 ms (Foltz 2013, Weis 2013). For this thesis, both the T2 of healthy prostate tissue and the longer T2 of cancerous prostate were modeled to test the limits of the UTE technique. The T1 time constant of the phantom was more than an order of magnitude

larger than the T2 time constant, so T1 was expected to have little influence on the UTE sequence.

### 3.2.2 Recipe and preparation of samples

Multiple material samples were created using variations of the recipe listed in Table 1 (Hattori 2013). These materials were dissolved in distilled water in the indicated quantities. The amount of agarose adjusted T2 while the amount of $GdCl_3$ altered T1. Of the remaining components, carrageenan assisted with gelatinization, NaCl altered the conductivity of the material, and $NaN_3$ retarded the growth of molds or other microorganisms in the material. All materials were purchased from Fisher Scientific (Fair Lawn, NJ), except carrageenan which was purchased from Research Products International (Mt Prospect, IL).

Table 1: Concentrations to produce prostate-like T1 and T2 behavior on a 3T MRI (Hattori 2013).

| | Prostate tissue phantom material composition | |
|---|---|---|
| | Suggested concentration by Hattori | Concentration used in this experiment |
| agarose | 0.714% w/w | 0.700% w/w |
| $GdCl_3$ | 22.2 μmol/kg | 22.2 μmol/kg |
| carrageenan | 3% w/w | 3% w/w |
| NaCl | 0.291% w/w | 0.200% w/w |
| $NaN_3$ | 0.03% w/w | 0.03% w/w |

Figure 3.1 illustrates the preparation steps. The ingredients were measured, and then dissolved in 97 mL of distilled water in a glass beaker to make 100 grams of prostate material. The mixture was heated to 90°C for 5 minutes in a hot water bath while continuously stirred. To prevent air bubbles from forming in the final phantom, the mixture was heated for an additional 20 minutes in the hot water bath without stirring. Each mixture was poured into a 7.5 cm

24

diameter plastic container and cooled to room temperature. The phantom material hardened upon

cooling and could then be removed from the container. A Foley catheter was inserted to model

the urethral opening in the center of the prostate phantom. The catheter was also used as a

marker for phantom orientation.
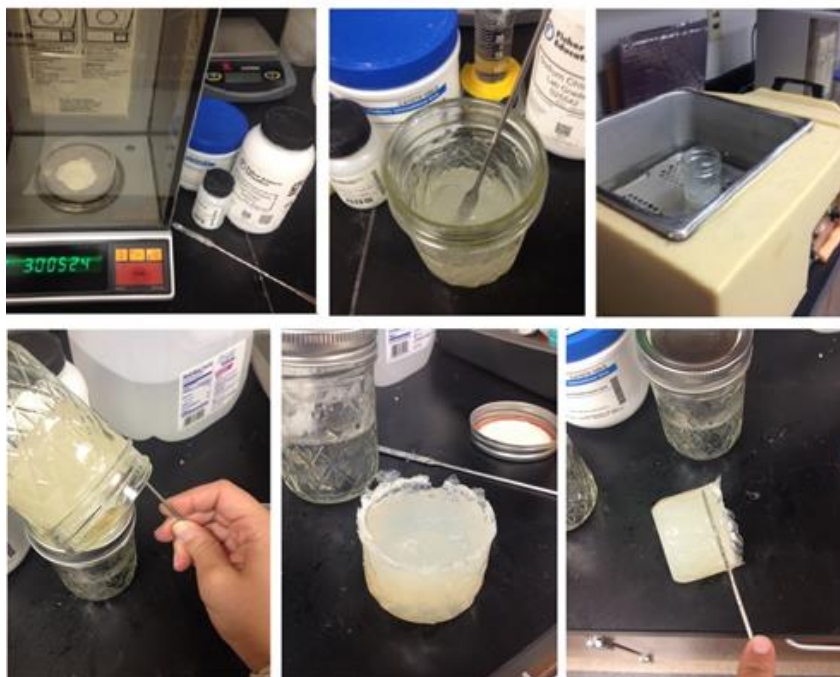


Figure 3.1: Steps of material preparation. Shown in the top row, (left) digital scale used to measure chemicals, (center) mixing of chemicals, and (right) heating in a water bath. Shown in the bottom row, (left) pouring mixture into a mold, (center) a solidified prostate phantom, and (right) needle insertion into the prostate phantom.

3.2.3 T1 and T2 validation tests

To measure the T1 time constant, the inversion recovery technique was used (Hornak 2014). MRI images were acquired of the phantom for 6 inversion times (TI) with all other parameters held constant. These parameters are listed in Table 2.

The images were loaded in MRmap (Messroghli 2012), a software program written in IDL (Exelis Visual Information Solutions, Boulder, CO); a screenshot is shown in Figure 3.2. To determine the T1 time constant, average signals were calculated for a region of interest placed

identically in the same slice of each inversion recovery image. The average signals were plotted versus signal collection time and the T1 decay curve was fit to the data. As mentioned previously, the T1 time constant was not expected to affect the UTE measurements, because T1 was at least an order of magnitude larger than T2.

Table 2: Parameters used to acquire inversion recovery images to measure the T1 relaxation time of the phantom materials.

| T1 time constant estimation protocol parameters | |
|---|---|
| TE (echo time) | 15.0 ms |
| TR (repetition time) | 15 s |
| TI (inversion time) | 1900,1600,1300, 800,600,500 ms |
| Echo train length (number of 180° rephasing pulses) | 16 |
| Receiver Bandwidth | ± 31.25 kHz |
| Field of View | 16.0 cm |
| slice thickness | 5.0 mm |
| slice spacing | 0.5 mm |
| Number of excitations | 0.5 |
| frequency encoding steps | 256 |
| phase encoding steps | 256 |
| frequency direction | R/L |

The T2 time constant was calculated with the multi-echo technique. In this technique, the same slice was imaged 8 times during one TR with varying echo times. The parameters for these scans are listed in Table 3. To measure the T2 time constant, an IDL-based software program called H.A.N.D.-Dynamic MRI software tool (Hoffman 2012) was used. This program plotted the signal intensity from each of the 8 images as a function of echo time for each pixel (Figure 3.3). An exponential decay curve of the net magnetization vector was fit to the graphed data points and the T2 time constant for each pixel was determined. The resultant T2 time constant values were averaged over a region of interest that was expected to be homogenous in the phantom.
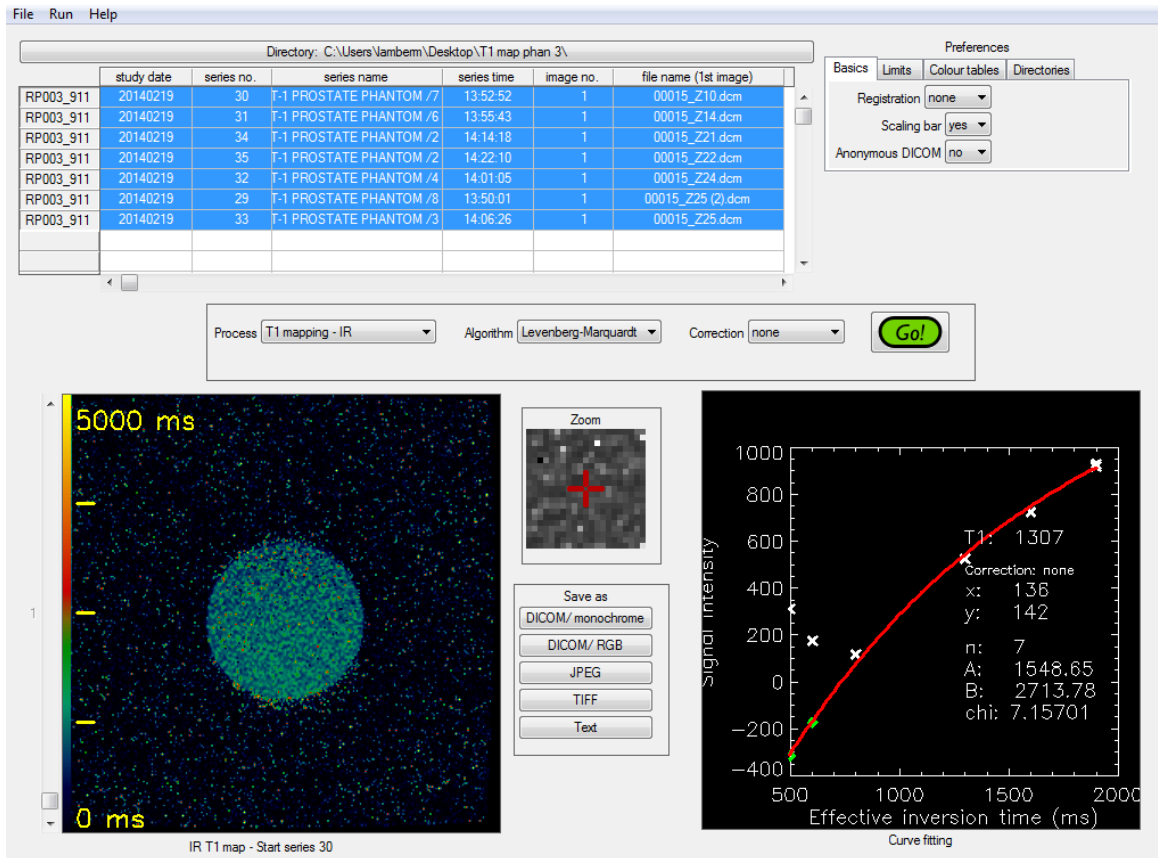
Figure 3.2: MRmap program used to estimate the T1 relaxation time of the phantom material (Messroghli 2012).

Table 3: Parameters used to acquire spin echo images to measure the T2 relaxation time of the phantom materials.

| T2 time constant estimation protocol parameters | |
|---|---|
| Number of echoes | 8 echoes |
| TE (echo time) | 7.26, 14.22, 21.34, 28.45, 35.56, 42.67, 49.78, 56.90 ms |
| TR (repetition time) | 1650 ms |
| TI (inversion time) | 50 ms |
| Receiver Bandwidth | ±62.5 kHz |
| Flip angle | 90 degrees |
| Field of View | 14.0 cm |
| slice thickness | 7.0 mm |
| slice spacing | 4.6 mm |
| Number of excitations | 1 |
| frequency encoding steps | 320 |
| phase encoding steps | 256 |
| frequency direction | R/L |
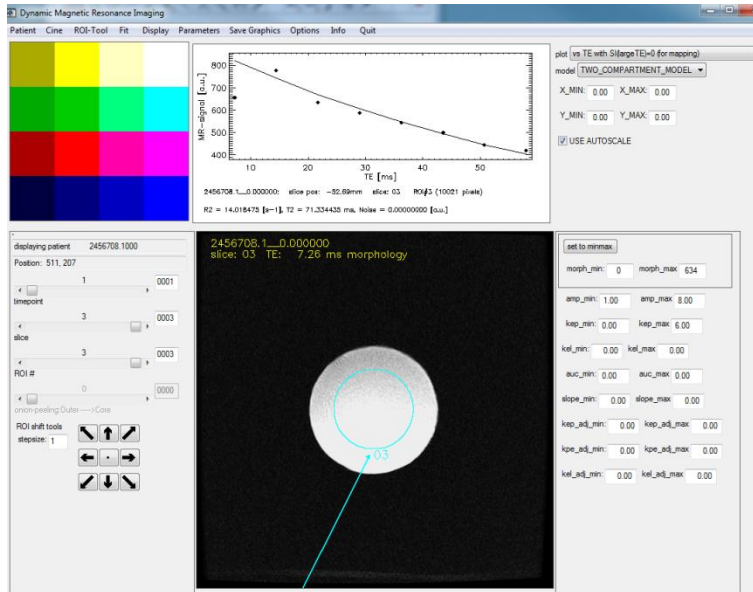
Figure 3.3: Screenshot of the software program, H.A.N.D, used to measure the T2 relaxation time of the phantom materials (Hoffman 2012). The first TE was not used for curve fitting.

### 3.2.4 T1 and T2 validation results

The right column of Table 1 lists the recipe that resulted in T1 and T2 values closest to the target values. T1-weighted and T2-weighted images for two representative materials are shown in Figure 3.4. These two materials represented a cancerous prostate with shortened T1 and lengthened T2 (Figure 3.4, left) and a healthy prostate with T1 and T2 close to the target values (Figure 3.4, right). The "healthy" prostate tissue had T2 of 79 ms (target of 74 ms) while the "cancerous" prostate had a T2 of 95 ms (target of 110 ms).

The measured T1 time constant for the "healthy" prostate was 1725 ms compared to the target of 1597 ms. The "diseased" prostate had a shorter T1 than planned at 795 ms; this was due to the difficulty of achieving a consistent T1 time constant. Small differences in the $GdCl_3$ concentration occurred because of the small quantity required. Although not intended, this material sample provided a means to see if a short T1 values would impact seed localization with

28
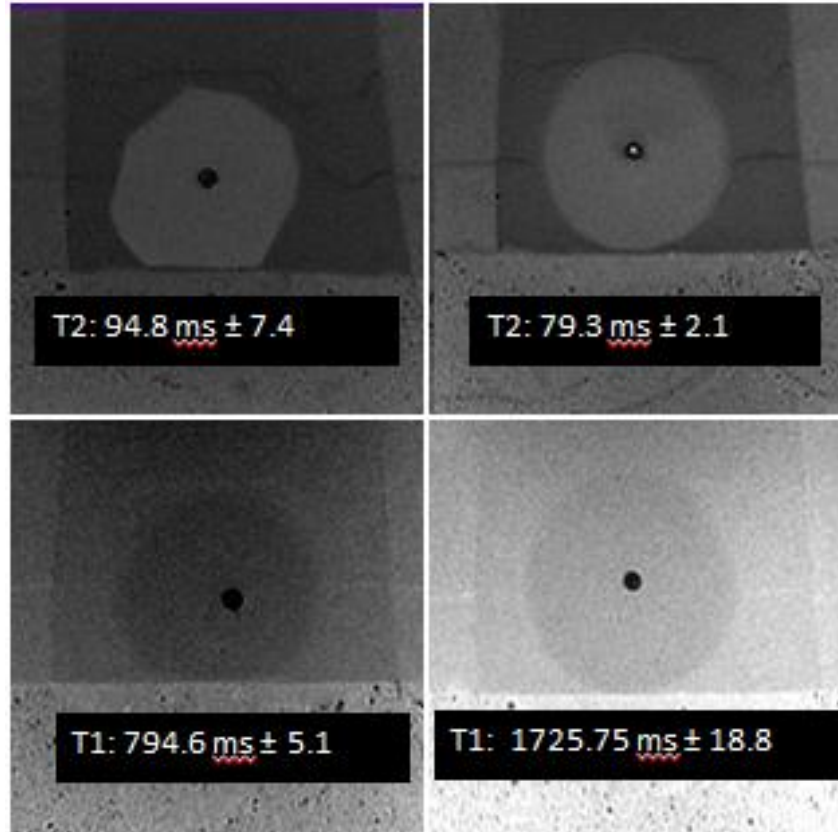
Figure 3.4: Average measured T1 and T2 relaxation times for two prostate phantoms; both of these samples were used in the pelvic phantom.

the UTE pulse sequence (see the results in Chapter 5). Both of these prostate samples were utilized in the pelvic phantom described in the next section.

3.3 Pelvic Phantom Fabrication

The pelvic phantom consisted of a polycarbonate box containing prostate and non-prostate tissue substitutes. The dimensions of the box were chosen to mimic reasonable pelvic dimensions. A total of 5 prostate phantoms were suspended in the phantom surrounded by non-prostate tissue; however, not all of the 5 prostate phantoms were used in subsequent analysis, as discussed at the end of this section.

A polycarbonate box with 6.4 mm thick walls was fabricated with inside dimensions of 30.5 cm wide, 20.3 cm tall, and 12.7 cm deep. The box was filled with a gelatin mixture that was

chosen to model the T1 and T2 values of muscle tissue. This material was mixed using concentrations suggested by (Hattori 2013) using the same materials as the prostate, but with altered concentrations to model T1 and T2 values of muscle (Table 4). This material was selected to represent the worst case scenario because the time constants are similar to prostate, but different enough for the two types of materials to be resolved on an MRI image. An initial layer of 7-8 mm of muscle substitute was poured into the box and allowed to solidify (Figure 3.5). Three prostate phantoms with values closest to the target T1 and T2 values were positioned axially along the center of the box. Then, additional muscle mixture was filled around the prostate phantoms so they remained suspended in the center of the field of view. The completed pelvic phantom is shown in Figure 3.6. Once the pelvic phantom was hardened, the gelatin material was solid enough to maintain its shape when removed from the polycarbonate box.

Table 4: Concentrations to produce muscle-like T1 and T2 behavior on a 3T MRI (Hattori 2013).

| Muscle tissue phantom material composition | | |
|---|---|---|
| | Suggested concentration by Hattori | Concentration used in this experiment |
| agarose | 1.187% w/w | 1.200% w/w |
| $GdCl_3$ | 30.1 µmol/kg | 55.0 µmol/kg |
| carrageenan | 3% w/w | 3% w/w |
| NaCl | 0.291% w/w | 0.291% w/w |
| $NaN_3$ | 0.03% w/w | 0.03% w/w |

During fabrications, spray cans were inset into the muscle tissue to create voids where other tissue substitutes could be added later if desired. Two additional prostate phantoms, pre-implanted with physically pre-determined seed positions, were set into one void. However, limitations in the available field of view of the UTE sequence precluded this portion of the phantom from being used in subsequent analysis.
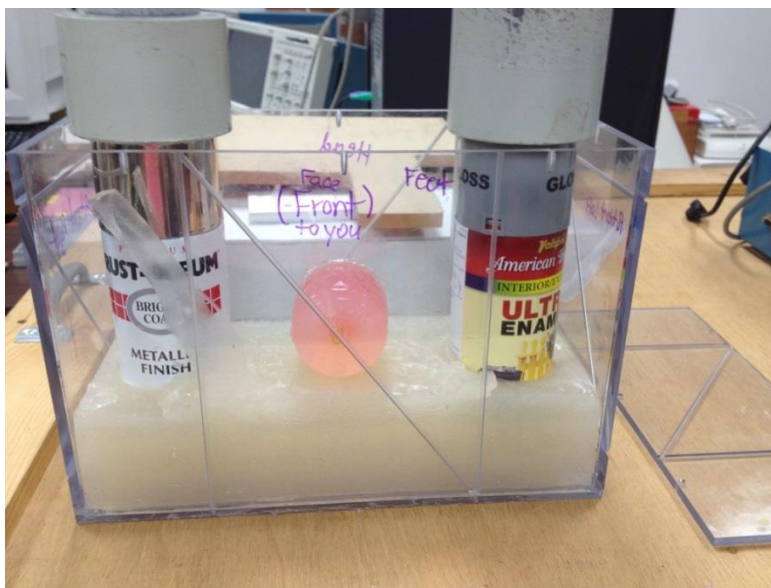
Figure 3.5: Creation of pelvic phantom. Three prostates were suspended in the center of the pelvic phantom (only one is shown in this photo). The spray cans were used to create voids for possible addition of other tissues.
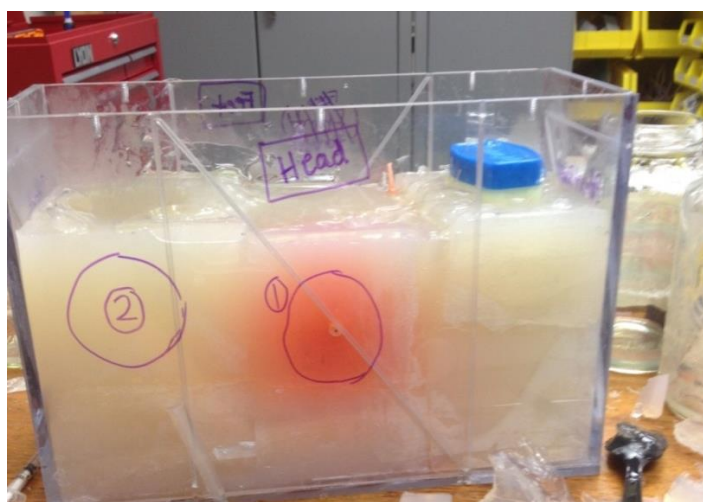


Figure 3.6: Pelvic phantom after fabrication was complete but before seed implantation.

Additionally, a jar of petroleum jelly was set into the other void in the pelvic phantom to assess possible heating of the titanium seeds by the UTE sequence. A seed was placed on the surface of the petroleum jelly. Excessive heating of the seed would soften the jelly, causing the seed to sink. The seed remained in its original location throughout the entire experiment indicating no significant heating of the seed.

3.4 Seed Implantation

Three types of seeds were used in this study, which were all decayed to greater than 10 half-lives; these included: (1) STM-1251 iodine-125 radioactive sources (BARD Medical, Inc), (2) AgX-100 iodine-125 (Theragenics), and (3) palladium-103 sources (Theragenics). The specifications of the STM-1251 I-125 source are shown in Figure 3.7 (Rivard 2004); a photo of a seed was shown in Figure 1.2.
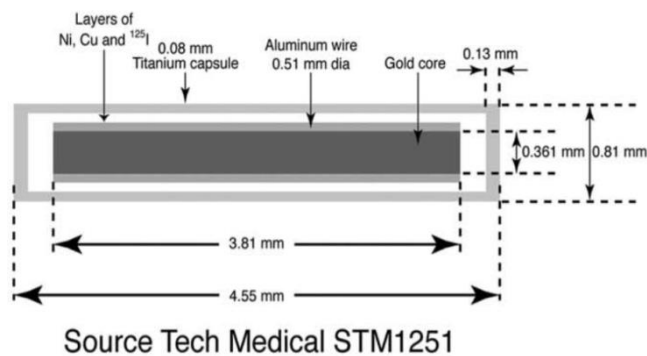


Figure 3.7: Specifications for the BARD brachytherapy seed used to model seed implantation in this project (Rivard 2004).

After removing the solidified pelvic phantom from the box, the brachytherapy seeds were implanted in the prostate phantoms located in the center of the pelvic phantom. The seeds were implanted using both standard spacing and random spacing as shown in Figure 3.8 and Figure 3.9. The seeds were implanted so they would be oriented parallel to $B_0$ when scanned in Aim 2. As discussed in section 1.3, every brachytherapy treatment is tailored to the patient's prostate size and shape; in a typical implant, seeds can be more concentrated in some areas and less in others. The most common method of seed implantation consists of each seed connected with a 5 mm spacer (Figure 3.9). Alternatively, seeds can be linked with 0.5 mm spacing. Both spacing arrangements were modeled in the pelvic phantom. Finally, single seeds were placed to represent deviations from intended placement, for use in Aim 3.

Figure 3.8: Steps for seed implantation. The seed strands before implantation and the needle used for seed implantation.
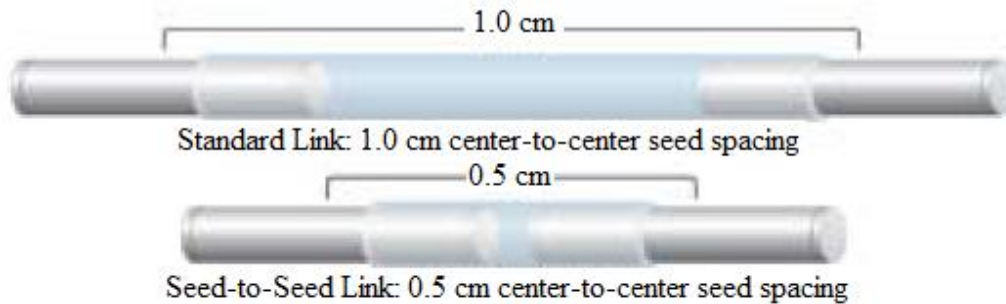


Figure 3.9: SourceLink spacers used to space the seeds in different configurations. The seed spacers were made of 70:30 poly(L-lacgtide-co-D,L-lactide). (BARD Medical)

### 3.4.1 Phase maps to assess $B_0$ distortion by titanium seeds

As a supplemental test for the proof of concept, a phase map was collected to map the phase differences throughout the pelvic phantom. As mentioned in section 2.5, each pixel in the phase map represents the magnitude of the difference in precessional frequency compared to the Larmor frequency.

Figure 3.10 (left) is a typical gradient-recalled echo image of the pelvic phantom with 10 seeds plus the urethra. Figure 3.10 (right) is the phase difference map of the same slice, which represents the difference between B and $B_0$. The large ring-shaped patterns at the right and left sides of the image are phase wrapping artifacts, which were explained in section 2.5. The phase difference increased dramatically in the vicinity of the seeds, due to magnetic susceptibility causing changes in local field strength. This large gradient contributes to chemical shift artifacts, which are described in Chapter 4 as a method to identify seeds.
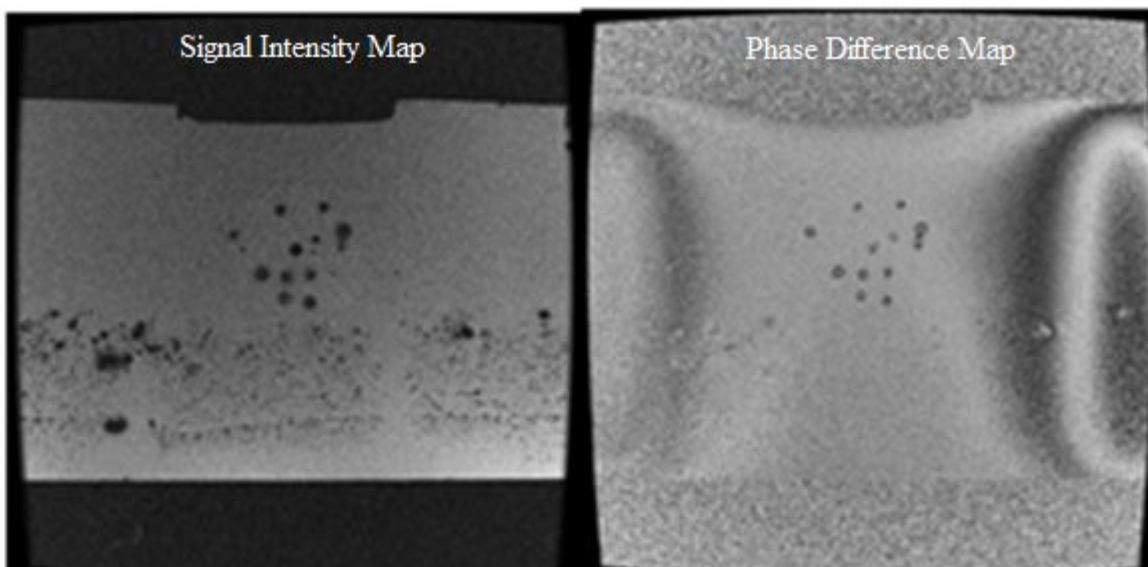


Figure 3.10: A gradient echo based image (left) and the corresponding phase difference map (right) of the pelvic phantom after the seeds were implanted.

The phase maps revealed that the $B_0$ is substantially distorted close to the seed's edge, a key aspect to the expected utility of the UTE sequence. In the phase map, seed locations could be identified, but metal did not appear different from other artifacts like air bubbles. This result indicated that phase maps themselves cannot be used to differentiate metal seeds from other non-metal artifacts.

3.5 Discussion

     After the seeds were implanted with the same needles used by physicians in a typical procedure, the gelatin was hardened enough not to reform around the needle tracks. This could have also contributed to errors with the introduction of air to the phantom material causing altered seed visualization. Seed trains over the entire length prostate phantom were used to minimize this error.

3.5.1  Seed placement

     The needles used to implant the brachytherapy seeds into the pelvic phantom were created to slightly bend when implanted into the prostate to enable the physician to counteract the swelling or resistance in the patient anatomy. As a result, the seeds were not implanted exactly in alignment with $B_0$. This is common for clinical procedures as well, but when combined with an inexperienced "surgeon", many seeds were implanted closer together than intended. This could lead to miscounts even with the gold standard counting method, CT (Lindsay 2003). In reality, the seeds would not be implanted in such a manner, so this represented the worst possible case scenario that modeled an unskilled implantation procedure. To remediate this error, a possible solution would be to have an experienced surgeon implant the seeds into the phantom, or use patient data that represents clinically acceptable seed spacing.

## CHAPTER 4: AIM 2, IMAGE ACQUISITION AND QUALITY ASSESSMENT

### 4.1 Overview

The goal of this aim was to acquire UTE MRI images to assess the utility of UTE for post-implant dosimetry. The quality of the images was assessed through qualitative and quantitative metrics. The final scan parameters were selected to help create post-implant dosimetry guidelines in Aim 3.

### 4.2 Materials and Methods

Using the pelvic phantom described in the previous chapter, MRI scans were collected to determine which pulse sequence parameters affect the quality of images to be used for post-implant dosimetry. The scanner used in this procedure was a 3T GE Signa HDxt MRI scanner with version 16.0 software located at Pennington Biomedical Research Center. The phantom was scanned with multiple parameter combinations that were compared qualitatively for best seed visualization. Then, the image quality was assessed using the following parameters: signal-to-noise ratio (SNR), contrast-to-noise ratio (CNR), signal contrast between seed and prostate tissue, and apparent seed diameter (with line profile).

### 4.2.1 Phantom setup

The phantom was oriented on the MRI scanner to match a typical prostate patient setup as closely as possible (Figure 4.1). An 8-channel torso array coil was used. The prostate phantom was centered in the field of view roughly 125 cm above the table.

### 4.2.2 UTE acquisition parameters

The 3D UTE pulse sequence used in this study was provided by Dr. Jiang Du from the Department of Radiology at the University of California, San Diego. The pulse sequence and reconstruction programs were loaded onto the PBRC MRI workstation. Program configuration

was edited to match the program code to be compatible with the software version of the PBRC

workstation. The UTE scan parameters are listed in Table 5.
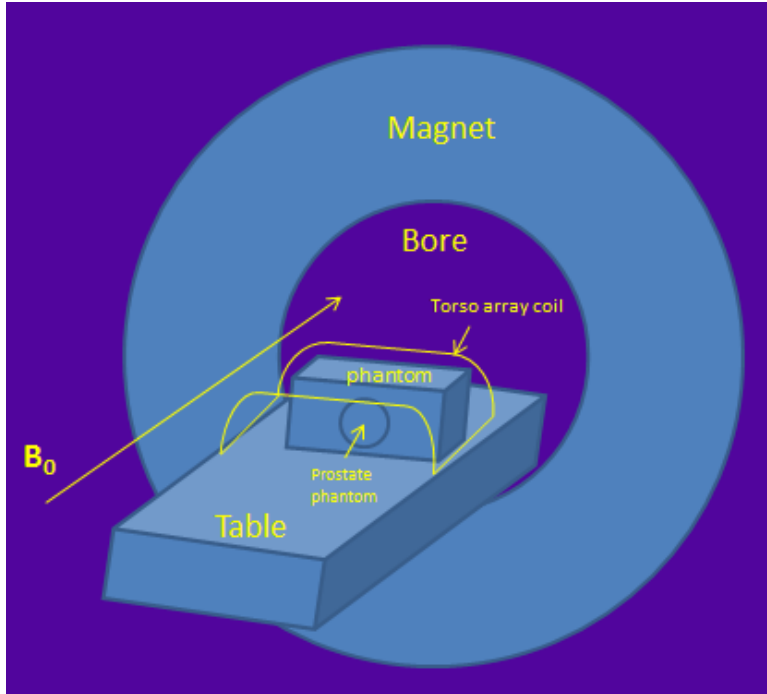


Figure 4.1: Illustration of the phantom setup in the MRI scanner.

Table 5: MRI parameters used to collect a UTE image of the pelvic phantom. (Personal communication with J. Du, UCSD, 2013).

| UTE parameters | |
|---|---|
| TR | 12 ms |
| TE | 30 μs or 60 μs |
| Receiver Bandwidth | ± 31.25 Hz, ± 62.5 Hz, or ± 125 Hz |
| Flip angle | 9 degrees, 14 degrees, or 30 degrees |
| Field of View (FOV) | 18.0 cm x 18.0 cm |
| Slice thickness | 0.7013 mm |
| Slice spacing | 0.7813 mm  (isotropic 3D resolution) |
| Frequency encoding steps | 256 |
| Phase encoding steps | 256 |
| Imaging plane | Axial |
| Number of radial k-space projections | 40,000 |

4.2.3 Fast Spin Echo acquisition parameters

Image data was also acquired with a fast-spin echo (FSE) pulse sequence. FSE was used for comparison because this is the most commonly used T2-weighted imaging sequence to provide adequate prostate soft tissue contrast (Bowes 2013). The FSE parameters are summarized in Table 6.

Parameters were chosen to match the typical clinical parameters for post-implant dosimetry. Only the FOV was specifically matched to the UTE parameters; other UTE scan parameters do not have an obvious parallels with FSE parameters. For example, the UTE sequence is 3D, while the typical FSE scan used for comparison was 2D. In particular, TE and TR were substantially different between UTE and FSE due to the unique nature of the UTE sequence.

Additionally, the bandwidth was different between the scans. The 3D nature of the UTE sequence required a shorter selection of bandwidth, while literature review of typical T2-weighted FSE scan parameters intended for post-implant dosimetry imaging suggested a higher bandwidth. For comparison, the "best case scenario" for each imaging sequence was selected. These best cases highlight the positive features and advantages of each pulse sequence.

Table 6: Recommended pulse sequence parameters to collect a T2-weighted image at 3T used for post-implant dosimetry (Bowes 2013).

| Fast spin echo parameters | |
|---|---|
| TE | 90 ms |
| TR | 3775 ms |
| ETL | 10 |
| Receiver BW | ± 20.8 kHz |
| FOV | 20.0 cm |
| slice thickness | 3 mm |
| slice spacing | 3 mm |
| frequency encoding steps | 320 |
| phase encoding steps | 224 |
| Frequency direction | R/L |

## 4.3 Results and Discussion

### 4.3.1 Signal pile-up phenomenon

Signal pile-up is a phenomenon that occurs when a tissue is imaged in proximity to a material with a large magnetic susceptibility, such as prostate tissue with implanted titanium brachytherapy seeds. As reviewed in section 2.3, applied gradients allow the data to be spatially sorted depending on the frequency of the net magnetization vector in each voxel. The magnetic susceptibility of adjacent materials changes the local B-field strength causing spins to precess at a rate different than the Larmor frequency. These spins are misplaced at a spatial position that is not the true physical location of the spins (Figure 4.2). Signal pile-up describes the magnitude of displaced signals registered to a specific voxel, causing a signal intensity difference from voxels that are more distant from the high-susceptibility material (Carl 2013).

$$\Delta x = \text{FOV}_x \frac{\Delta \omega}{\text{full BW}} \tag{4.1}$$

Equation 4.1 describes the relationship between the distance of the spatial shift ($\Delta x$), the field of view in the readout direction (FOVx), the shift in frequency ($\Delta \omega$), and the full bandwidth (e.g. rBW of $\pm$ 16 kHz = full BW of 32 kHz).
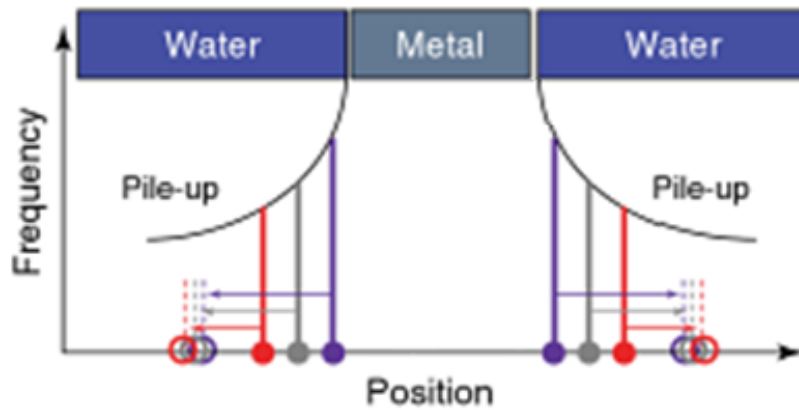


Figure 4.2: Illustration of the signal pile-up effect where signal is shifted spatially to a falsely represented location in the spatial position image (Bydder 2012).

This effect is illustrated in Figure 4.3 for image data acquired in this project, where sagittal views of 3 seeds from two UTE image acquisitions are shown. The FOV of the first trial (Figure 4.3, left) was 2 cm larger than the second trial (Figure 4.3, right), with bandwidth and other parameters held constant. The appearance of the pile-up effect was completely inverted, as illustrated in the cartoons below the UTE images. This showed that the relationship between FOV and $\Delta x$ strongly impacts the appearance of the seeds, which could result in misinterpretation of seed locations.
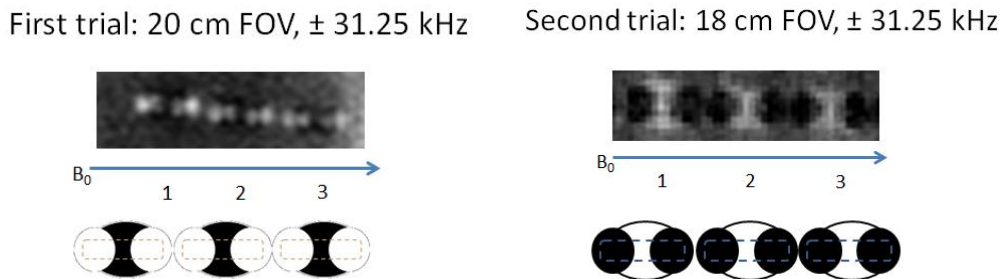


Figure 4.3: Sagittal view of 3 seeds from two trials of UTE acquisition, with (top) 20 cm FOV compared to (bottom) 18 cm FOV. The cartoons illustrate where the pile up occurred relative to the centers of the seeds.

4.3.2  Apparent seed size

One parameter used to quantify the pile-up effect was apparent seed diameter, which was essentially the diameter of the pile-up artifact. As discussed previously, a brachytherapy seed itself does not provide signal on a proton-based MRI scan, due to the lack of hydrogen in the titanium implant. However, the pile-up effect shifted tissue signals immediately adjacent to the titanium seeds, which was visualized with UTE. The signal pile-up from the protons immediately adjacent to the seeds resulted in positively contrasted, or bright, borders for the seeds. This susceptibility artifact occurs in all MRI images with metallic implants, but the visualization of the artifact is usually lost with the conventional use of relatively long TE; seeds show up as black

voids indicative only of a lack of spins because the susceptibility artifact de-phases too quickly before the signal can be acquired. UTE captures the pile-up signal before it can be lost.

The apparent seed diameter was used to quantify the amount of pile-up effect. Seed diameter was determined as the full width at half maximum of the seed in a line profile, comparing the peak in the line profile to the average noise level. The line profile across a seed was measured with the line profile tool in ImageJ (Rasband 1997-2014). The line profiles are shown in Figure 4.4 for one seed in UTE and FSE images of an implanted prostate phantom. Figure 4.5 plots the line profiles on the same graph to emphasize the greatly increased signal magnitude in the UTE image due to the susceptibility artifact.

Based on 80 seed measurements, the average apparent seed diameter measured on the T2 weighted FSE image was $1.46 \pm 0.38$ mm. The apparent seed diameter increased with increasing bandwidth on the FSE image. For the same 80 seeds measured on the UTE images, the average apparent seed diameter was $4.65 \pm 0.63$ mm. The exaggerated seed diameter made the seeds more visually apparent. This could lead to improvement of seed counting accuracy which will be discussed in Aim 3.
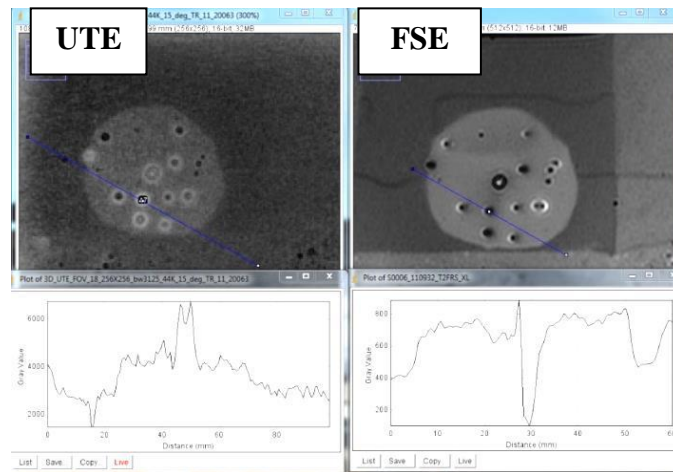


Figure 4.4: Line profile measurements measured in ImageJ (Rasband 1997) for the same slice in both UTE and FSE images. The line profiles plot pixel intensity along the blue line in each image.
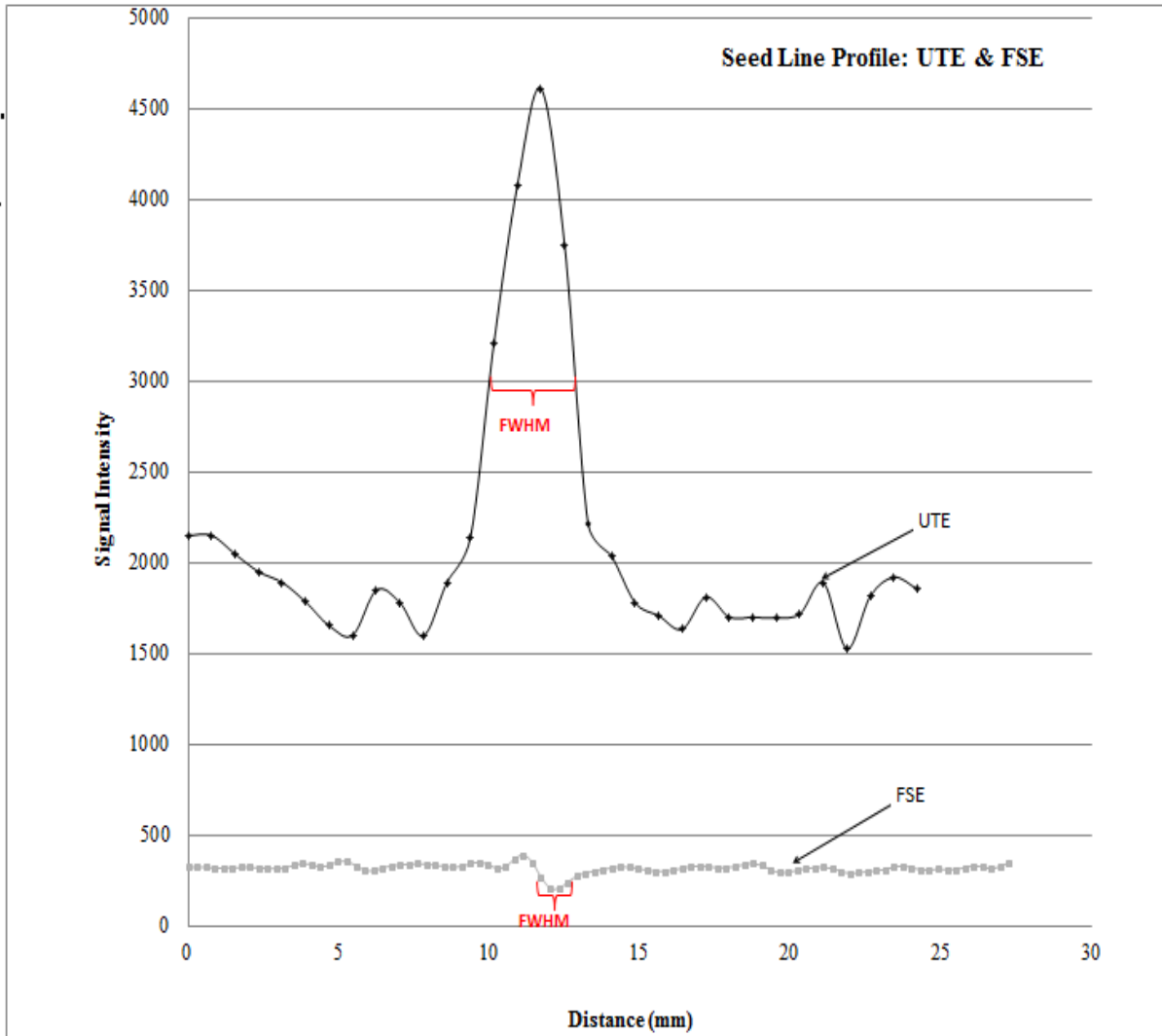
Figure 4.5: Line profiles for the same seed from both FSE and UTE displayed on the same scale. This graph illustrates the ability of UTE to capture the large signal magnitude due to pile-up.

## 4.4 Discussion of UTE Parameter Variations

### 4.4.1 Receiver bandwidth

Changes in receiver bandwidth altered apparent seed size. The pile-up intensity appeared to increase with lower bandwidth. As seen in Figure 4.6, for the same slice as well as the same window and level adjustments, when the bandwidth was varied, the seeds appeared larger and brighter for the lower bandwidth. This was a result of the relationship between shift size and

bandwidth for individual frequency offsets (Equation 4.1). The relationship between SNR and receiver bandwidth is:

$$SNR = \text{Voxel Volume} \sqrt{\frac{\text{Number of Measurements}}{\text{Bandwidth}}} \qquad (4.2)$$

which illustrates how a larger bandwidth resulted in a decrease in the pile-up effect for the same slice in a UTE image.
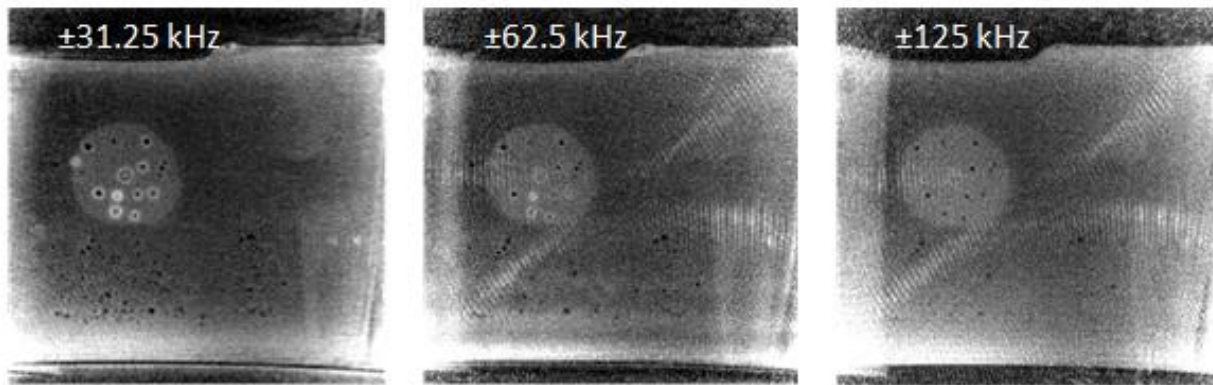


Figure 4.6: Three different receiver bandwidths used to acquire the same image slice with UTE. Note how the appearance of the bright ring (pile-up artifact) around a seed decreases with increasing bandwidth.

The lowest bandwidth was selected at ± 31.25 kHz because another relationship that affects the image quality is the relationship between TE and rBW. TE increases as rBW decreases. Too small of an rBW (a shallow linear gradient) causes the TE to increase (to fit the whole gradient) to too high of a value, reducing the ability of UTE to capture the magnetic susceptibility artifact.

4.4.2 Flip angle

Another user-defined parameter that affected image quality was flip angle. A smaller flip angle (the amount that $M_0$ is perturbed from the z-axis) forces a shorter signal collection time, but a large flip angle reduces the ability to see pile-up effects because the susceptibility-induced

T2 shortening results in signal decay prior to signal acquisition (after the RF pulse is completed). Variations in the flip angle showed that the signal pile-up effect was most intense visually for a flip angle of 15 degrees (Figure 4.7). This relationship can be explained by the Ernst angle.
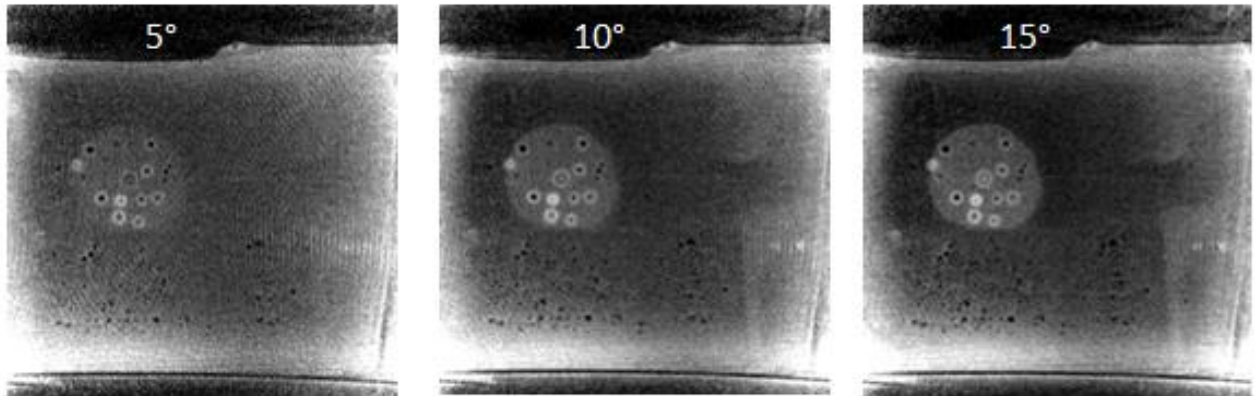


Figure 4.7: Three different flip angles used to acquire the same image slice with UTE.

The Ernst angle relationship is the flip angle for a spin that give the maximum signal intensity in the shortest amount of time (Haacke 1999). This flip angle is dependent on the TR and T1 relaxation time of the imaged tissue. The Ernst angle ($\alpha_E$) is given by:

$$\alpha_E = \arccos(e^{-TR/T1}) \tag{4.3}$$

and illustrated in Figure 4.8. For the "healthy" and "diseased" prostate phantoms imaged in this experiment, the Ernst angles were 7° and 10°. An interesting observation was that the images acquired at 15° appear to display more contrast between the prostate material and the pile-up artifact surrounding the seeds, although this results from the decrease in prostate signal with flip angle rather than a change in pile-up artifact.

Because the seed presented as a bright signal, the higher contrast between seed and prostate occurred when the prostate material was *not* at its maximum value. Therefore, using a flip angle just above the Ernst angle caused the seed to appear with more contrast. Unfortunately,
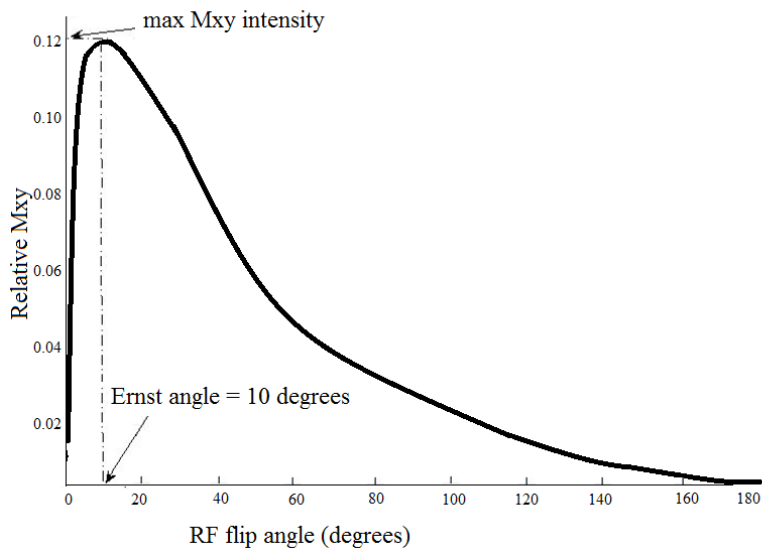
Figure 4.8: Relative transverse signal intensity as a function of flip angle. The Ernst angle is flip angle where the signal intensity is highest.

too large of a flip angle leads to a long TR, causing acquisition time to be too long for a convenient patient scan time. Therefore a flip angle of 15 degrees was selected.

4.5 UTE and FSE Comparison

UTE and T2-weighted FSE images were compared. Various parameters were selected for quantitative comparison including signal-to-noise ratio (SNR) and contrast-to-noise ratio (CNR). Additionally, qualitative parameters were examined including seed visibility and artifacts.

4.5.1 Regions of interest

To measure SNR and CNR between various sections on the UTE images, a region of interest was drawn on each slice. A sample of a few of the hundreds of regions of interest drawn to collect the data are shown in Figure 4.9.

4.5.2 SNR

The SNR was compared for the UTE and FSE images with the same bandwidth (Table 7). The SNR was measured with regions of interest within the prostate phantom adjacent to the

seed and in air. SNR was calculated as the average signal intensity of the prostate ROI divided by the standard deviation of air ROI:

$$SNR = \frac{average\ signal\ intensity}{standard\ deviation\ of\ the\ signal} \tag{4.4}$$

The average seed SNR for the UTE images was 15.99 ± 1.52, which was independent of bandwidth. The average seed SNR for the FSE images was 32.32 ± 22.43. Although the SNR was higher for the FSE image, this did not mean the seed contrast or visibility was better. In fact, the seed visibility was better in the UTE image, due to the bright ring surrounding each seed due to pile-up. The decreased SNR for the UTE sequence hindered prostate boundary definition, which means UTE does not easily provide both seed visualization and prostate delineation simultaneously. Accuracy of prostate delineation was not studied in this project, but should be considered for future work.
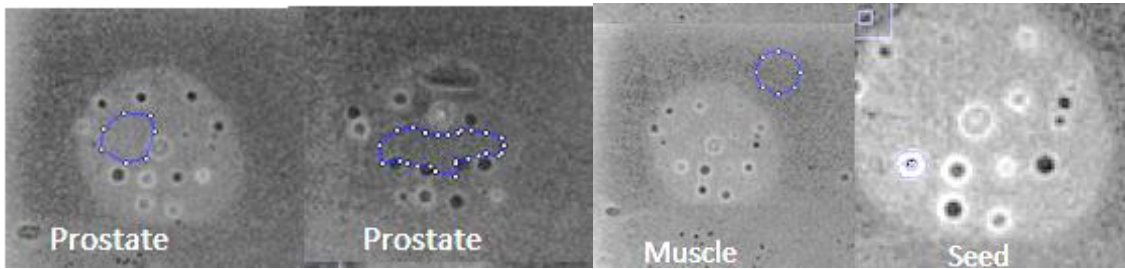


Figure 4.9: Samples of the regions of interest drawn with ImageJ (Rasband 1997) to collect signal intensities and standard deviation. These values were used to calculate SNR and CNR.

Table 7: Average measured SNR and CNR for both UTE and FSE images.

|  | UTE Phantom 1 | UTE Phantom 2 | FSE Phantom 1 | FSE Phantom 2 |
|---|---|---|---|---|
| SNR: Seed/noise | 17.62 ± 1.11 | 14.36 ± 1.04 | 33.47 ± 18.45 | 31.16 ± 12.76 |
| SNR: Prostate/noise | 11.25 ± 0.72 | 7.26 ± 0.78 | 73.83 ± 1.98 | 54.92 ± 1.65 |
| CNR | 6.37 ± 1.32 | 7.09 ± 1.30 | 4.04 ± 18.65 | 23.76 ± 12.87 |

### 4.5.3 CNR

The CNR was calculated for both UTE and FSE images. The CNR was measured with a ROI surrounding the seed, an ROI in the prostate tissue phantom near the seed, and an ROI in air. CNR was calculated as the ratio of the difference between the average prostate signal intensity and the average seed signal intensity to the standard deviation of those measurement regions:

$$CNR = \ SNR(prostate) - SNR \ (seed) \tag{4.5}$$

Listed in Table 7, the average CNR for the UTE images with $\pm$ 31.25 kHz bandwidth was 6.73 $\pm$ 1.85. The average CNR for the FSE images was 23.76 $\pm$ 12.87. Although the CNR was larger for the FSE image, seeds cannot be distinguished from air because both present as signal voids.

### 4.5.4 Qualitative assessment

Qualitatively, overall seed visibility appeared to be better with UTE. This was attributed to the bright ring-shaped pile-up artifact around the seed. At very short echo times, the positive contrast visualization of the seeds was clearly distinct from the appearance of other artifacts (e.g. air cavities) due to the different magnitudes of magnetic susceptibility. The phase difference maps in Figure 4.10 showed that the highest change in susceptibility in fact appeared near air bubbles. However, air bubbles should not be present within the prostate in vivo and in any case would be unlikely to have the same size as seeds.

The slice montage in Figure 4.11 shows the formation of a seed signal as compared to the formation of an air bubble signal (Figure 4.12). The arrows show the bright center of the seed in between slices with a bright ring. Also, the arrows show an air bubble that is similar in size to a seed; the air bubble lacks the bright center, indicating an artifact rather than a seed.
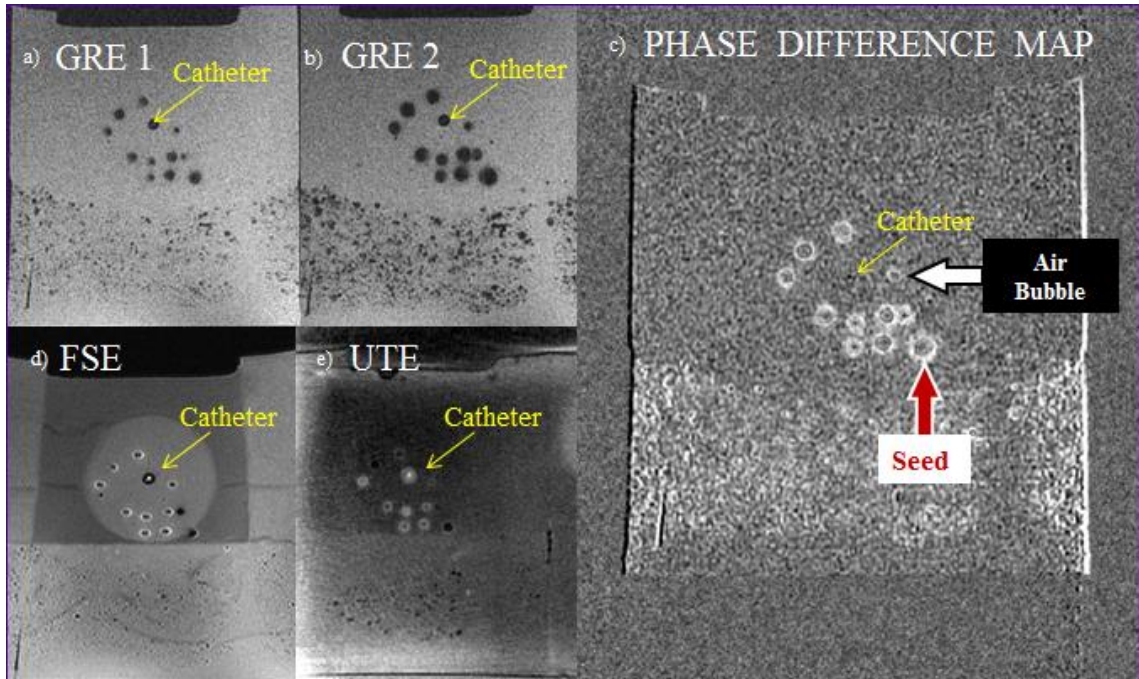
Figure 4.10: Gradient-recalled echo images a) with TE: 2.25 ms and b) TE: 5.8 ms and all other parameters held constant of the same slice in the pelvic phantom. Phase difference map c) of the same slice. This map was collected using concepts discussed in section 2.5. Corresponding d) FSE and e) UTE images of the same slice in the pelvic phantom.

4.5.5 Statistical significance of seed ROI

Table 8 lists the results of performing a Student's t-test on the average SNR results for seeds, prostate phantom tissue, and air. The results show that the seed signal was significantly different both from the phantom's prostate tissue and from air. This supported the hypothesis of this project regarding the ability of UTE to generate a signal due to brachytherapy seeds that is different from the surrounding prostate tissue and from other artifacts.
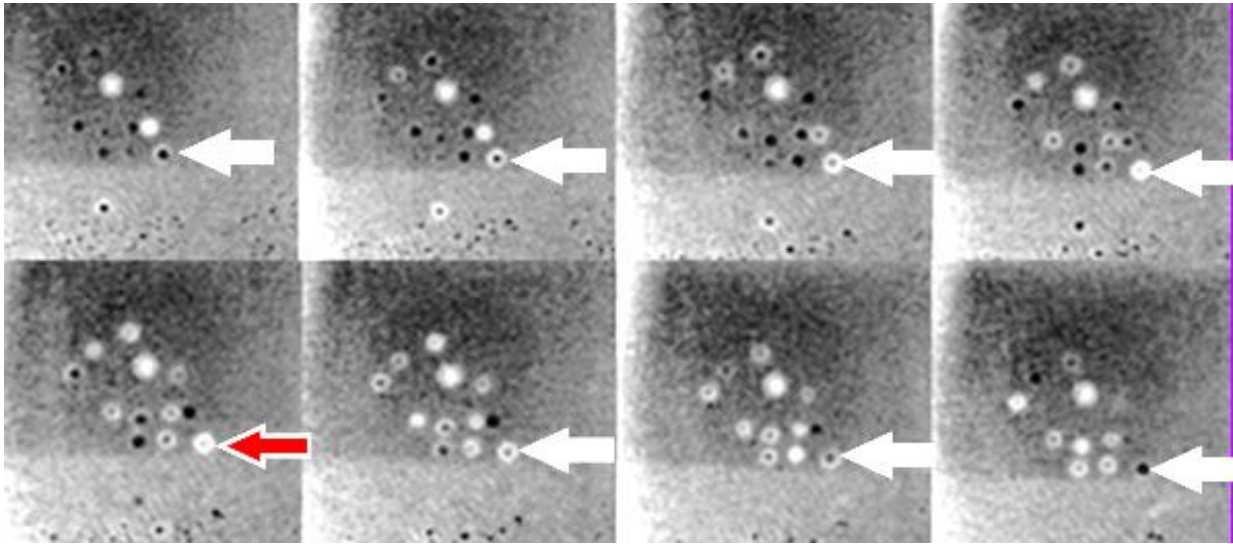
Figure 4.11: A seed (white arrow) on 8 consecutive slices (0.7013 mm thick). The red arrow shows where the pile-up in the center of the ring that is used to identify the presence of a seed on the UTE image.
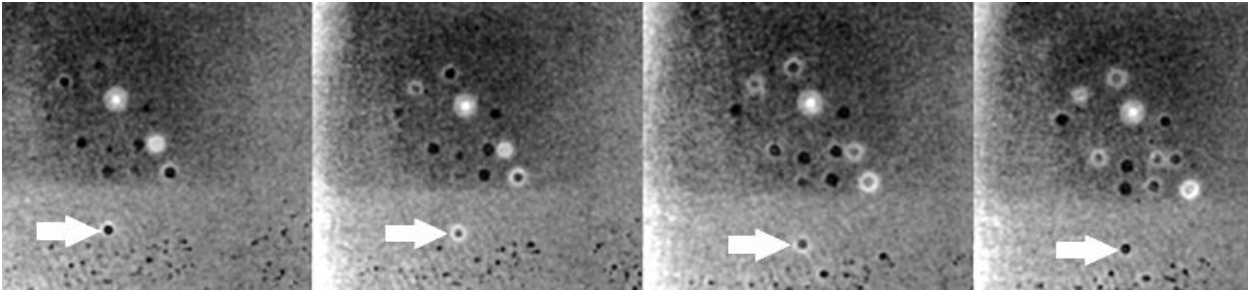


Figure 4.12: An air bubble (white arrow) on 4 consecutive slices (0.7013 mm thick). This shows the lack of bright center that the seed characteristically displays on the same scan.

Table 8: Results from Student's t-test performed on the average SNR results for seed prostate and air signal.

| Hypothesis | Corresponding p values |
|---|---|
| Seed signal> prostate signal | $p < 0.05$ |
| Seed signal > air signal | $p < 0.001$ |

# CHAPTER 5: AIM 3, SEED LOCALIZATION PROCEDURE AND RECONSTRUCTION ACCURACY

## 5.1  Overview

The goal of this aim was to develop guidelines for brachytherapy seed counting with the UTE MRI pulse sequence. Instructions were drafted that described how to identify seeds based on the observations of seed appearance (artifacts) reported in Chapter 4. Two experienced physicists counted the seeds on the same set of phantom images. The purpose of this aim was to establish a baseline method that could be subsequently refined for investigation with patient data.

## 5.2  Materials and Methods

The images collected from Aim 2 were used to develop criteria for identifying seeds. In the future, an automatic seed localization program may be conceivable, but such development was outside the scope of this project.

### 5.2.1  Seed configuration

The pelvis phantom was implanted with 18 strands of titanium seeds that mimicked common seed distributions in patient plans. The seeds were connected using BARD spacers as shown in Figure 3.9; one configuration consisted of seeds spaced equally apart, shown in the lower part of Figure 5.1. A variety of configurations was implanted to test the capabilities of UTE imaging to identify seeds in different geometries.

### 5.2.2 Characteristics of seed appearance on UTE images

The center of a seed appeared as a bright white spot. On the superior and inferior axial slices, a seed appeared to have a central black spot bordered with a thick white ring. Figure 5.2, Figure 5.3 and Figure 5.4 show an illustration prepared to train observers in the appearance of seeds and other structures in a UTE image.
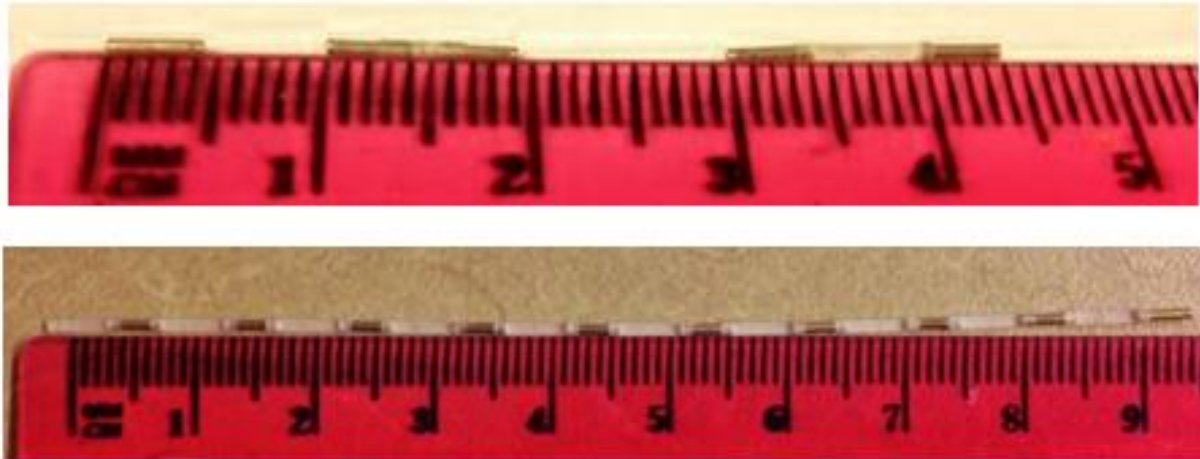
Figure 5.1: Seed configurations implanted. The varied configuration (top) was used to test the seed localization accuracy and the standard configuration (bottom) was used for reference.
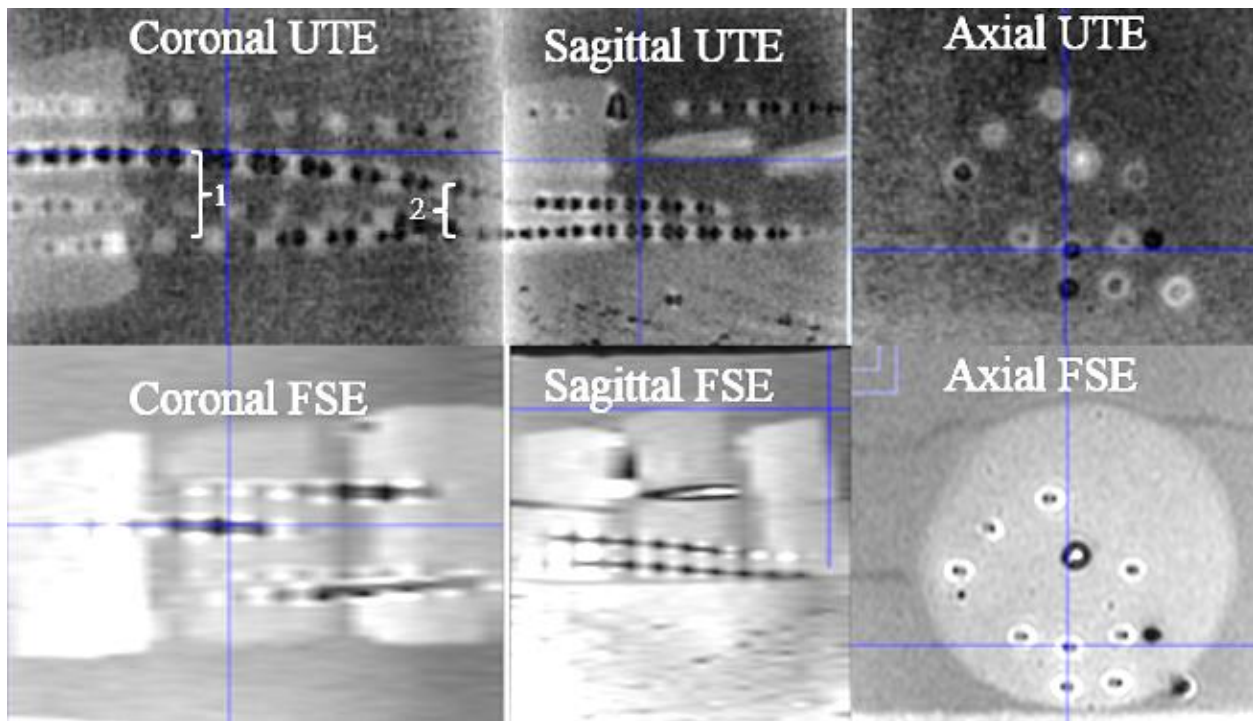


Figure 5.2: Comparative orthogonal views of the same location on both UTE and FSE images. The spacing between the beginning of two seed strands (1) is almost double the spacing towards the end of the same two seed strands (2) as highlighted in the Coronal UTE image
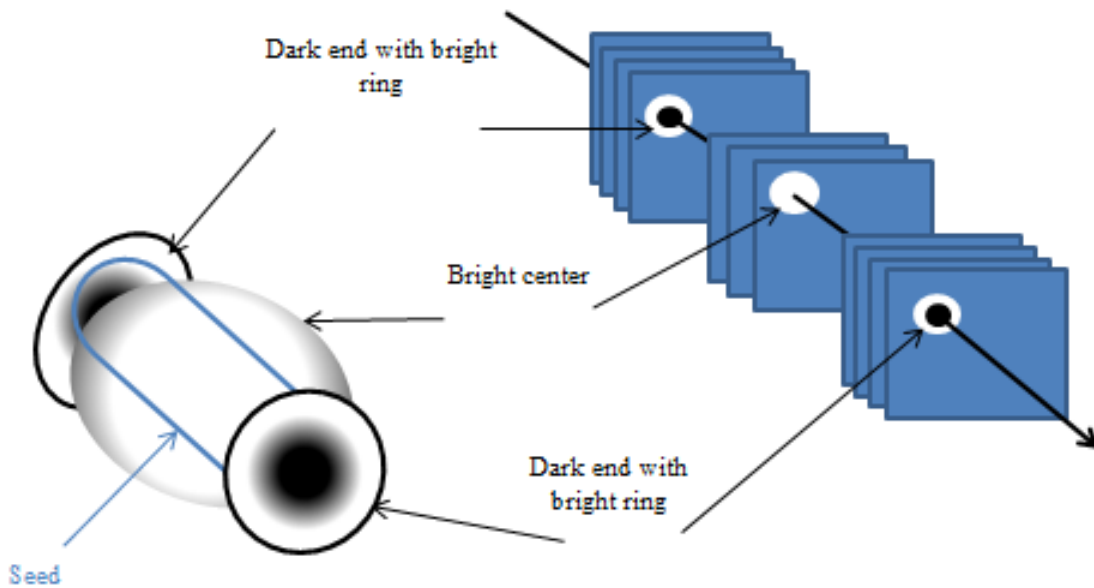
Figure 5.3: An illustration used to explain how a seed will appear to observers in UTE images. The dark black arrow on the right of the illustration shows how the slices would be scrolled through in the axial direction.
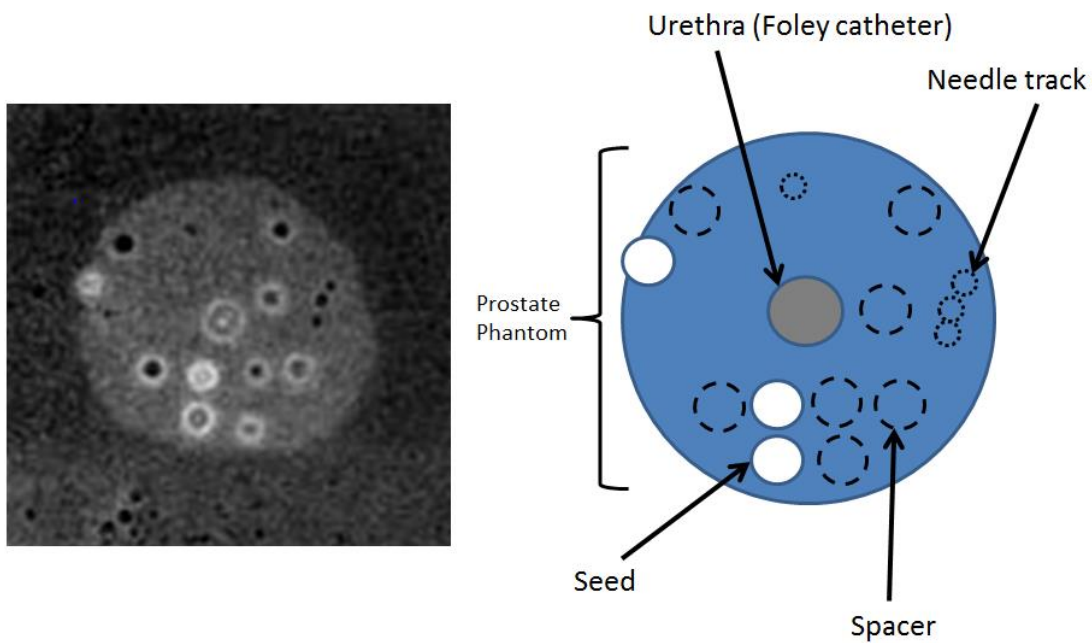


Figure 5.4: Description (right) of what is visible on a sample UTE slice (left) shown to observers as training for seed counting.

5.2.3 Seed counting guidelines

Two physicists experienced in post-implant dosimetry for prostate brachytherapy volunteered to participate in this experiment. The physicists were given directions for seed identification on ImageJ (Rasband 1997-2014). The instructions were:

A seed will always have a bright ring before and after the bright white center. If you see a ring not followed by a bright white center, it is an artifact. Some seeds have a tiny white dot in the center which indicates the center of the seed. Not all seeds have this. Some are simply a solid white spot. Both are considered a seed to be counted. When two seeds are implanted without a spacer between them, the signal pile-up effect is compromised, and appears slightly different than if there was a spacer between the two.

Step 1: Locate the seed in the axial view using the yellow cursor (cf. Figure 5.5).
Step 2: Confirm the seed is positioned within a strand using the corresponding orthogonal views (cf. Figure 5.6).

Representative images that accompanied the instructions are shown in Figure 5.5 (for Step 1) and Figure 5.6 (for Step 2).
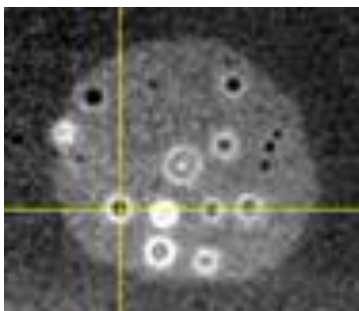


Figure 5.5: Axial view of seed on UTE image. The yellow cursor is centered on the seed by the observer.
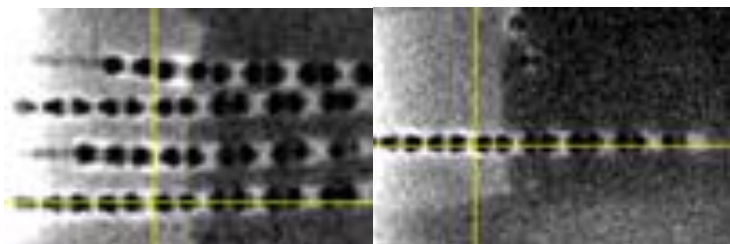


Figure 5.6: The corresponding coronal (left) and sagittal (right) views of the seed centered in Figure 5.5.

## 5.3 Results and Discussion

### 5.3.1 Exclusion of slices at edge of FOV

When the final UTE scans were collected, an unanticipated artifact was seen in the slices adjacent to the polycarbonate walls of the pelvis phantom (Figure 5.7). Slices near the box walls exhibited an elevated intensity, strongest adjacent to the box walls and decreasing with distance from the wall. This elevated intensity masked the appearance of the main attribute of the seeds in the UTE sequence. Bright pixel values indicate shortened T2 in this region. However, it was uncertain if the artifact was caused directly by the polycarbonate material (i.e. the polycarbonate influenced the apparent T2 of the phantom material), if polycarbonate has an ultra-short T2 component of its own, or if the phantom material solidified in a structured manner due to proximity to the polycarbonate that caused a reduction in T2. Regardless of the cause, the 10 slices adjacent to each polycarbonate wall, where this artifact was apparent, were excluded from the slices used to test the feasibility with physicists counting the seeds.
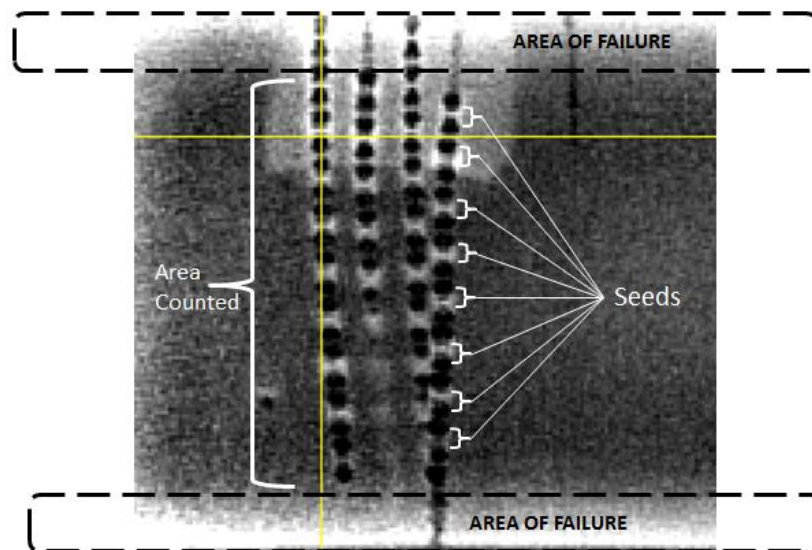


Figure 5.7: Area of elevated signal intensity due to the contamination of ultra-short T2 signal from the polycarbonate walls of the pelvic phantom. The outlined areas (labeled "Area of Failure") were excluded in the localization tests

## 5.3.2 Physicists' counting results

Table 9 gives the results of seed counting by two physicists who were experienced in brachytherapy seed localization with CT. For comparison, also listed are the seed counts determined by the author from the UTE images and from CT by VariSeed™ (Varian Medical Systems, Inc., Palo Alto, CA). VariSeed™ is commercial product supported by many years of optimization. The similar counts obtained by the physicists, without optimization of the UTE sequence for the desired task, indicated the promise of UTE for brachytherapy seed localization. Note that the author implanted the seeds and was able to visually inspect the phantom; this seed count is considered the true count.

Table 9: Results of the seed localization test performed by 2 physicists and the author of this work.

| Subject | UTE Seed Counts |
|---|---|
| Physicist 1 | 86 |
| Physicist 2 | 83 |
| Author of this work | 90 |
| CT + VariSeed™ | 89 |

## 5.4 Discussion

The best visual results came from seeds that were implanted at the center of the pelvic phantom. As advised by an experienced UTE MRI physicist (Du, private communication), the main area of interest should be placed at the center of the FOV. This is due to the nature of the UTE pulse sequence collection scheme (Carl 2013).

The border of the prostate phantom against the background material was difficult to see with the same window/level as used for seed counting (Figure 5.8). Changing the window and

level helped to visualize the prostate border, although the border was always better evident in FSE images.
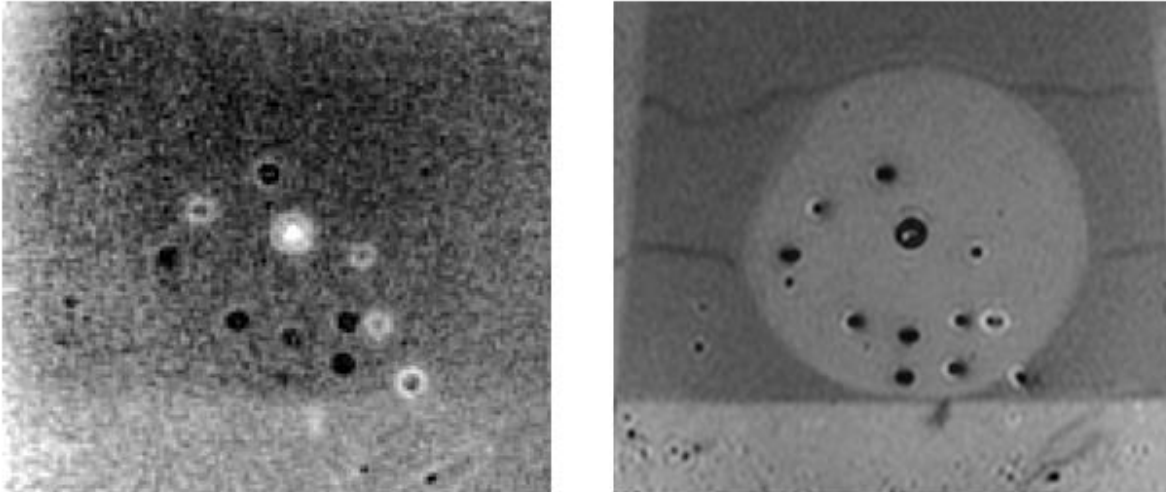


Figure 5.8: A selected slice with poor prostate definition on the UTE image (left) and slightly improved prostate definition on the corresponding FSE image (right).

The seed counts exceeded 92% accuracy for all users, compared to reported seed localization accuracies of about 70% with other post-implant MR sequences (Bowes 2013). This method did not achieve the 100% accuracy desired from post-implant dosimetry imaging (Bowes et al. 2013), but as noted previously, the UTE parameters used here were selected as best guesses and were likely not optimal. One observation was the background signal's interference with the seed signal appearance in areas with a high signal present from the prostate phantom with a short T1 relaxation time (795 ms compared to the accepted 1600 ms for prostate tissue). This short T1 was not wholly representative of prostate tissue, but the observation was interesting because it indicated that seeds present in a tissue with a short T1 relaxation time would be more difficult to visualize; combined with the small FOV necessary for acceptable patient imaging times, this may have implications for detecting seeds that have migrated out of the prostate.

An addition to the procedure, suggested by one physicist, was to use the orthogonal views to help confirm seeds versus artifacts. It proved advantageous to use an orthogonal view of the seeds because the distinct pattern of the seeds in the sagittal plane helped clarify the reader's uncertainty. Orthogonal views are not typically used with other methods for seed counting (fusion or CT) due to thicker slices with poor seed definition in the axial direction.

The use of the 3D UTE sequence could be a significant factor to improve the accuracy of seed localization on MRI. A 3D scans provides isotropic resolution with good seed definition in all directions, while the distinctive pile-up effect can be captured with UTE.

5.4.1 Patient scans of UTE without seeds

In Figure 5.9, a healthy patient was scanned with the UTE protocol parameters acquired with 5° and 20° flip angles from Table 5. Both images in Figure 5.9 used the same echo time (30 μs). The smaller flip angle resulted in a noiser image; both images showed the presence of bright short-T2 areas surrounding the prostate that could potentially interfere with seed localization. Further UTE studies of patients with implanted seeds are required to investigate how realistic patient anatomy will affect seed localization accuracy with UTE.
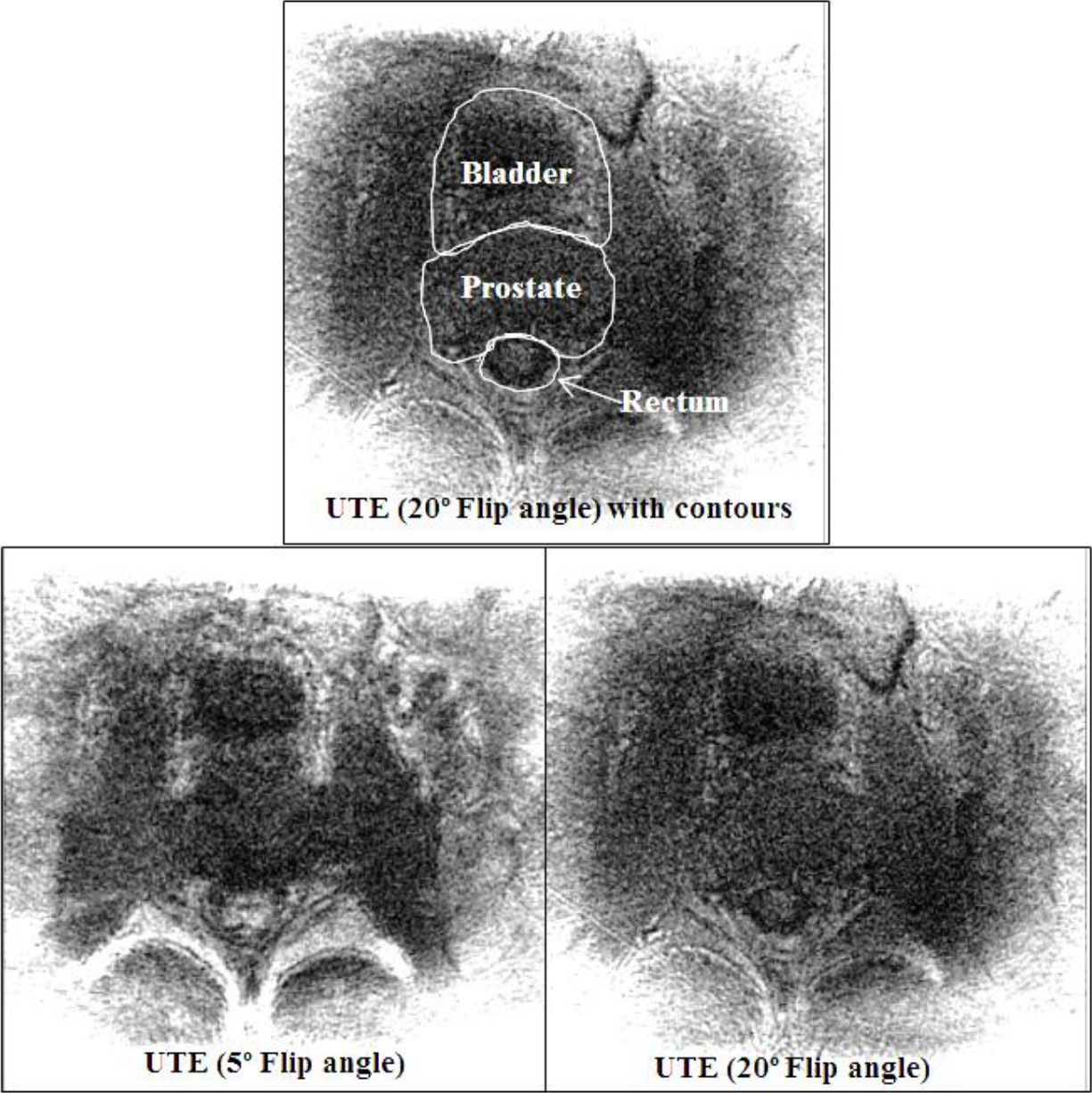
Figure 5.9: UTE scans of the prostate of a healthy volunteer. The top image shows contours of the prostate, bladder and rectum for the same patient in the bottom images.

CHAPTER 6: CONCLUSION

6.1 Summary of results

      This study demonstrated that UTE is a feasible alternative for localizing titanium prostate brachytherapy seeds after implantation, specifically BARD STM-6711 iodine-125 seeds. Results indicated that UTE-based post-implant images were sufficient to differentiate seeds from artifacts caused by the presence of air bubbles ($p<0.05$) and prostate ($p<0.001$). The ability to accurately identify seed from non-seed material is critical for MR-based post-implant dosimetric calculations. Prostate delineation quality for UTE images was decreased compared to FSE. Overall, UTE imaging yielded image sets with apparently sufficient differentiation to facilitate seed localization for post-implant permanent brachytherapy seed dose calculations in the prostate.

6.2 Response to hypothesis

      UTE was capable of differentiating titanium seeds from prostate and air bubble artifacts, evidenced by the statistically significant increased signal from the titanium seeds on UTE when compared to the signal from both prostate ($p<0.001$) and air ($p<0.05$). The results of this project led to the conclusion that the UTE pulse sequence is better than T2-weighted FSE MRI for seed identification because it distinctively visualized metallic seeds from air bubbles and prostate tissue. However, the UTE pulse sequence was worse than FSE in terms of SNR, which led to an ambiguous prostate outline on the UTE image. Additionally, the apparent diameter of the seeds localized on the UTE scan was much larger than the true diameter; while helpful for qualitative visualization, how this might quantitatively impact dosimetric results was not studied.

6.3 Recommendation

      This study clearly demonstrated the potential utility of UTE for visualization of brachytherapy seeds, using acquisition parameters identified from the literature on UTE in other

applications. An optimum imaging protocol should be developed through a more complete survey of UTE parameter space. At this time, we recommend that the UTE pulse sequence be used for manual seed identification, in conjunction with T2-weighted MRI for prostate delineation. The UTE pulse sequence is not recommended as a stand-alone imaging technique; in particular, UTE requires a relatively small field of view, which may limit its utility for situations where seeds have migrated out of the prostate. As mentioned, a complete survey of parameter space, including aspects of bandwidth and field of view, would be a valuable extension of this work.

6.4 Limitations of the study

This feasibility study used UTE acquisition parameters that were based on application of UTE to situations other than the prostate, with a limited investigation of overall parameter space. As such, these parameters were likely not optimal for visualization of seeds with appropriate field of view, bandwidth, imaging time, etc. This study only modeled two variations of prostate tissue (with different T1 and T2 relaxation constants) in a homogeneous phantom, and did not include a variety of complications that may be encountered in vivo, e.g. calcifications and blood clots. These confounding factors could impact a UTE-based localization technique. While one could conceive of further phantom-based studies that include additional relaxation constants, more complex anatomy, or other complicating facets; moving to an in vivo study seems most appropriate for future studies.

6.5 Future work

As mentioned previously, a thorough survey of parameter space is recommended for protocol optimization. This survey should likely be a combination of phantom and in-vivo

imaging assessment. Of particular interest will be the parameters that directly affect seed appearance (for instance, receiver bandwidth) and SNR or CNR.

Spatial distortions for the UTE sequence should also be characterized. As noted, some seed trains appeared curved in the UTE images. Some needle deflection was likely caused by the flexibility of the implantation needle and the relatively stiff phantom material. Although the pelvis phantom was fabricated with alignment marks on the box, the limited field of view in the feasibility study was too small to include the marks, thus precluding an assessment of spatial non-uniformity in UTE scans.

Another area of possible investigation is task-based assessment of seed localization and its impact on dosimetric accuracy. This would require UTE images of many prostate seed implants; multiple readers would determine seed locations and orientations. Accuracy could be assessed with the localization data itself or with post-implant plans calculated from the localization data. Along with this, the distinctive pattern of the seeds in the UTE images suggests the possibility of developing an automated localization algorithm.

Finally, the literature reports that a number of pulse sequences are being investigated for prostate imaging, such as diffusion-weighted imaging or contrast-enhanced MRI (Tanaka 2006, Katayama 2011, Bowes 2013). However, these protocols focus on imaging of the prostate for diagnosis. The ability (or lack thereof) of these pulse sequences to visualize brachytherapy seeds should be investigated and compared to UTE.

REFERENCES

Bowes, D., Crook, J. M., Araujo, C., Batchelar, D. (2013). "Ultrasound-CT fusion compared with MR-CT fusion for postimplant dosimetry in permanent prostate brachytherapy." Brachytherapy **12**(1): 38-43.

Bowes, D., Crook, J. M., Rajapakshe, R., Araujo, C., Parker, B. (2013). "Defining a magnetic resonance scan sequence for permanent seed prostate brachytherapy postimplant assessment." Brachytherapy **12**(1): 25-29.

Brown, A. P., Pugh, T. J., Swanson, D. A., Kudchadker, R. J., Bruno, T. L., Christensen, E. N., van Vulpen, M., Frank, S. J. (2013). "Improving prostate brachytherapy quality assurance with MRI-CT fusion-based sector analysis in a phase II prospective trial of men with intermediate-risk prostate cancer." Brachytherapy **12**(5): 401-407.

Bydder, G. M., Fullerton, G. D., Young, I. R. (2012). MRI of Tissues with Short T2s or T2*s. Chichester, West Sussex, UK, John Wiley & Sons, Ltd.

Carl, M., Koch, K., Du, J. (2013). "MR imaging near metal with undersampled 3D radial UTE-MAVRIC sequences." Magn Reson Med **69**(1): 27-36.

CDC (2013). "Prostate Cancer" Cancer Prevention and Control, Centers for Disease Control and Prevention.

Crook, J. M., Patil, N., Ma, C., McLean, M., Borg, J. (2010). "Magnetic resonance imaging-defined treatment margins in iodine-125 prostate brachytherapy." Int J Radiat Oncol Biol Phys **77**(4): 1079-1084.

Davis, B. (2012). "American Brachytherapy Society Consensus Guidelines for Transrectal Ultrasound-guided Permanent Prostate Brachytherapy." Brachytherapy **11**(1): 6-19.

De Brabandere, M., Hoskin, P., Haustermans, K., Van den Heuvel, F., Siebert, F. A. (2012). "Prostate post-implant dosimetry: interobserver variability in seed localisation, contouring and fusion." Radiother Oncol **104**(2): 192-198.

De Brabandere, M., Kirisits, C., Peeters, R., Haustermans, K., Van den Heuvel, F. (2006). "Accuracy of seed reconstruction in prostate postplanning studied with a CT- and MRI-compatible phantom." Radiother Oncol **79**(2): 190-197.

Dubois, D., Bice, W., Prestige, B. (2001). "CT and MRI derived source localization error in a custom prostate phantom using automated image coregistration." Medical Physics **28**(11): 2280.

Foltz, W. D., Wu, A., Chung, P., Catton, C., Bayley, A., Milosevic, M., Bristow, R., Warde, P., Simeonov, A., Jaffray, D. A., Haider, M. A., Menard, C. (2013). "Changes in apparent

diffusion coefficient and T2 relaxation during radiotherapy for prostate cancer." <u>J Magn Reson Imaging</u> **37**(4): 909-916.

Haacke, E. M., Brown, R. W., Thompson, M. R., Venkatesan, R. (1999). <u>Magnetic Resonance Imaging Physical Principles and Sequence Design</u>. Hoboken, NJ, US, John Wiley & Sons, Inc.

Hattori, K., Ikemoto, Y., Takao, W., Ohno, S., Harimoto, T., Kanazawa, S., Oita, M., Shibuya, K., Kuroda, M., Kato, H. (2013). "Development of MRI phantom equivalent to human tissues for 3.0-T MRI." <u>Med Phys</u> **40**(3): 032303.

Hoffman, D. U. (2012). H.A.N.D.-Dynamic Magnetic Resonance Imaging Software Tool. The Ohio State Universtity Department of Radiology.

Hornak, J. P. (2014). The Basics of MRI. Rochester, NY, USA, Chemistry and Imaging Science at Rochester Insititute of Technology. **2014**.

Howlader, N., Noone, A. M., Krapcho, M., Garshell, J., Neyman, N., Altekruse, S. F., Kosary, C. L.,Yu, M., Ruhl, J., Tatalovich, Z., Cho, H., Mariotto, A., Lewis, D. R., Chen, H. S. (2013) "SEER Cancer Statistics Review, 1975-2010 (based on November 2012 SEER data submission, posted to the SEER web site, 2013)."

Katayama, N., Takemoto, M., Yoshio, K., Katsui, K., Uesugi, T., Nasu, Y., Matsushita, T., Kaji, M., Kumon, H., Kanazawa, S. (2011). "T2*-weighted Image/T2-weighted Image Fusion in Postimplant Dosimetry of Prostate Brachytherapy." <u>Journal of Radiation Research</u> **52**(5): 680-684.

Kuo, N., Lee, J., Tempany, C., Stuber, M., Prince, J. (2010, Apr 14). "Mri-Based Prostate Brachytherapy Seed Localization." <u>Proc IEEE Int Symp Biomed Imaging</u>, 2010, from http://www.ncbi.nlm.nih.gov/pubmed/21151846.

Lindsay, P., Van Dyk, J., Battista, J. (2003). "A systematic study of imaging uncertainties and their impact on [sup 125]I prostate brachytherapy dose evaluation." <u>Medical Physics</u> **30**(7): 1897.

Messroghli, D. (2012). MRmap v 1.4. Cardiovascular Imaging Group Deutsches Herzzentrum Berlin, Congenital Heart Disease and Pediatric Cardiology.

Nag, S., Bice, W., DeWyngaert, K., Prestidge, B., Stock, R., Yu, Y. (2000). "The American Brachytherapy Society Recommendations for Permanent Prostate Brachytherapy Postimplant Dosimetric Analysis." <u>Int. J. Radiaiton Oncology Biol. Phys.</u> **46**(1): 221-230.

Nath, R., Anderson, L., Luxton, G., Weaver, K., Williamson, J., Meigooni, A. (1994). "Dosimetry of interstitial brachytherapy sources: Recommendations of the AAPM Radiation Therapy Committee Task Group No. 43." <u>Med. Phys.</u> **22**(2): 209.

Rasband, W. S. (1997-2014). ImageJ. Bethesda, Maryland, USA, U.S. National Institute of Health.

Rivard, M., Coursey, B., DeWerd, L., Hanson, W., Huq, M., Ibbott, G., Mitch, M., Nath, R., Williamson, J. (2004). "Update of AAPM Task Group No. 43 Report: A revised AAPM protocol for brachytherapy dose calculations." Medical Physics **31**(3): 633.

Robson, M., Bydder, G. M. (2003). "Magnetic Resonance: An Introduction to Ultrashort TE (UTE) Imaging." J Comput Assist Tomogr **27**(6): 825-846.

Tanaka, O., Hayashi, S., Matsuo, M., Sakurai, K., Nakano, M., Maeda, S., Kajita, K., Deguchi, T., Hoshi, H. (2006). "Comparison of MRI-based and CT/MRI fusion-based postimplant dosimetric analysis of prostate brachytherapy." Int J Radiat Oncol Biol Phys **66**(2): 597-6002.

Tempany, C., Franco, F. (2012). "Prostate MRI: Update and current roles." Applied Radiology **41**(3): 17-22.

Weis, J., Ortiz-Nieto, F., Ahlstrom, H. (2013). "MR Spectroscopy of the Prostate at 3T: Measurements of Relaxation Times and Quantification of Prostate Metabolites using Water as an Internal Reference." Magnetic Resonance in Medical Sciences **12**(4): 289-296.

Melissa Lamberto was born in Philadelphia, Pennsylvania, and raised in Sicklerville, New Jersey. She attended the University of the Sciences in Philadelphia and received a Bachelor of Science degree in physics in 2011. In August of that same year, Melissa enrolled in the Graduate School at Louisiana State University to work towards her Master of Science degree in Medical Physics. In July 2014, Melissa will enter the medical physics residency program at the Helen F. Graham Cancer Center of the Christiana Care Health System located in Christiana, Delaware.